HR 5907: Discovery of the most rapidly rotating magnetic early B-type star by the MiMeS Collaboration★†

J. H. Grunhut,[1,2]‡ Th. Rivinius,[3] G. A. Wade,[2] R. H. D. Townsend,[4]
W. L. F. Marcolino,[5] D. A. Bohlender,[6] Th. Szeifert,[3] V. Petit,[7] J. M. Matthews,[8]
J. F. Rowe,[9] A. F. J. Moffat,[10] T. Kallinger,[8,11] R. Kuschnig,[8,11] D. B. Guenther,[12]
S. M. Rucinski,[13] D. Sasselov,[14] W. W. Weiss[12] and the MiMeS Collaboration

[1]*Department of Physics, Engineering Physics & Astronomy, Queens University, Kingston, Ontario K7L 3N6, Canada*
[2]*Department of Physics, Royal Military College of Canada, PO Box 17000, Station Forces, Kingston, Ontario K7K 7B4, Canada*
[3]*ESO - European Organisation for Astronomical Research in the Southern Hemisphere, Casilla 19001, Santiago 19, Chile*
[4]*Department of Astronomy, University of Wisconsin-Madison, 2535 Sterling Hall, 475 N Charter Street, Madison, WI 53706, USA*
[5]*Universidade Federal do Rio de Janeiro, Observatório do Valongo Ladeira Pedro Antônio, 43, CEP 20080-090, Rio de Janeiro, Brazil*
[6]*National Research Council of Canada, Herzberg Institue of Astrophysics, 5071 West Saanich Road, Victoria, BC V9E 2E7, Canada*
[7]*Department of Geology & Astronomy, West Chester University, West Chester, PA 19383, USA*
[8]*Department of Physics and Astronomy, University of British Columbia, 6224 Agricultural Road, Vancouver, BC V6T 1Z1, Canada*
[9]*NASA Ames Research Center, Moffett Field, CA 94035, USA*
[10]*Dépt. de Physique, Université de Montréal, C.P. 6128, Succursale: Centre-Ville, Montréal, QC H3C 3J7, Canada*
[11]*Institut für Astronomie, Universität Wien, Türkenschanzstrasse 17, A-1180 Wien, Austria*
[12]*Institute for Computational Astrophysics, Department of Astronomy and Physics, Saint Marys University, Halifax, NS, B3H 3C3, Canada*
[13]*Department of Astronomy and Astrophysics, University of Toronto, 50 St George Street, Toronto, ON M5S 3H4, Canada*
[14]*Harvard−Smithsonian Center for Astrophysics, 60 Garden Street, Cambridge, MA 02138, USA*

ABSTRACT

We report the discovery and analysis of a very strong magnetic field in the rapidly rotating early B-type star HR 5907, based on observations obtained as part of the Magnetism in Massive Stars (MiMeS) project. We infer a rotation period of $0.508\,276^{+0.000\,015}_{-0.000\,012}$ d from photometric and Hα EW measurements, making this the shortest period, non-degenerate, magnetic massive star known to date. From the comparison of *IUE* UV and optical spectroscopy with LTE BRUCE/KYLIE models we find a solid-angle integrated, uniform black-body temperature of $17\,000 \pm 1000$ K, a projected rotational velocity of $290 \pm 10\,\mathrm{km\,s^{-1}}$, an equatorial radius of $3.1 \pm 0.2\,R_\odot$, a stellar mass of $5.5 \pm 0.5\,M_\odot$, and an inclination angle of the rotation axis to our line-of-sight of $70 \pm 10°$. Our measurements of the longitudinal magnetic field, which vary between -500 and -2000 G, phase coherently with the rotation period and imply a surface dipole field strength of $\sim$15.7 kG. On the other hand, from fits to mean Least-Squares Deconvolved Stokes *V* line profiles we infer a dipole field strength of $\sim$10.4 kG. This disagreement may result from a magnetic configuration more complex than our model, and/or from the non-uniform helium surface abundance distribution. In either case we obtain a magnetic obliquity nearly aligned with the rotation axis ($\beta = 7^{+2}_{-1}°$). Our optical spectroscopy also shows weak variability in carbon, silicon and nitrogen lines. The emission variability in hydrogen Balmer and Paschen lines indicates the presence of a dense, highly structured magnetosphere, interpreted as a centrifugally supported, magnetically confined circumstellar disc.

Key words: techniques: photometric – techniques: polarimetric – stars: circumstellar matter – stars: individual HR 5907 – stars: magnetic field – stars: rotation.

1 INTRODUCTION

Since stars more massive than $\sim 2\,M_{\odot}$ lack a significant convective envelope, which is a necessary ingredient to drive a solar-type dynamo, magnetic fields are not expected to be observed in these stars. However, the chemically peculiar, intermediate mass Ap/Bp stars have been known for over half a century to host strong, globally organized magnetic fields with surface strengths of up to tens of kG (e.g. Borra & Landstreet 1973). At the hotter end of the Bp star class are the main sequence, He-strong stars (e.g. Bohlender et al. 1987) that show significant enhancement and often variability in their helium lines, as is found in the archetypical star σ Ori E (e.g. Landstreet & Borra 1978) and the recently discovered star HR 7355 (Oksala et al. 2010; Rivinius et al. 2010). In addition to the helium variability, some He-strong stars show emission variability in Balmer lines, photometric brightness variations, variable ultraviolet (UV) resonance lines, and non-thermal radio emission, most of which vary with a single period, interpreted to be the rotational period of the star (e.g. Pedersen & Thomsen 1977; Walborn 1982; Shore & Brown 1990; Leone & Umana 1993). Many of these phenomena are thought to be due to the presence of a rigidly rotating, centrifugally supported magnetosphere – a region in the circumstellar environment where the stellar wind couples to the magnetic field and is forced to co-rotate with the star (Shore & Brown 1990; Townsend & Owocki 2005).

The subject of this paper, HR 5907 (HD 142184, V1040 Sco), is a bright ($V = 5.4$), early type B2.5V (Hoffleit & Warren 1991), emission line star with a high $v \sin i$ ($340\,\mathrm{km\,s^{-1}}$; Frémat et al. 2005). HR 5907 is located in the nearby Upper Scorpius OB association at a distance of ~ 145 pc (Hernández et al. 2005).

This star was originally brought to the attention of the Magnetism in Massive Stars (MiMeS) collaboration (Wade et al. 2011) because of its $P \sim 0.5$ d *Hipparcos* photometric variability (Hubert & Floquet 1998), which would be in good agreement with the expected rotation period for a star of this spectral type and $v_{\mathrm{eq}} \sin i$, and would imply that HR 5907 would be the most rapidly, or possibly second most rapidly, rotating magnetic B-type star (North, Babel & Lanz (1988) reported a photometric period ($P = 0.475518 \pm 0.000059$ d) of the photometrically variable late B-type star HD 60431 in IBVS that has yet to be confirmed through magnetic or spectroscopic measurements). Additionally, archival FEROS spectra suggested that the observed Hα profile is morphologically more similar to the profiles of other magnetic He-strong stars (such as σ Ori E or HR 7355) than to classical Be stars.

In this paper we report on the discovery and first detailed investigation of the magnetic field and spectral variability properties of HR 5907. In Section 2 we discuss the details of the observed spectroscopic, spectropolarimetric and photometric data, while in Section 3 we re-examine the photometric and Hα variability to refine the period. The fundamental parameters are evaluated in Section 4 and the spectral variability is analysed in Section 5. In Section 6 we constrain the magnetic field strength and geometry using the polarimetric data. In Section 7 we examine the properties of the magnetosphere and present a discussion of this study in Section 8.

2 OBSERVATIONS

2.1 Polarimetry

Between 2010 February and 2011 March, 27 high-resolution ($R \sim 68\,000$) spectropolarimetric (Stokes I and V) observations of HR 5907 were collected with the ESPaDOnS spectropolarimeter at the Canada-France-Hawaii Telescope (CFHT) as part of the survey component of the MiMeS large program. Each spectropolarimetric observation consists of four individual subexposures that were processed using the UPENA pipeline running LIBRE-ESPRIT, following the double-ratio procedure as described by Donati et al. (1997) to produce the Stokes I and V spectra. Null polarization spectra were also produced by combining the individual four subexposures in such a way that the polarization should cancel out (Donati et al. 1997). This allows us to verify whether spurious signals are present in our reduced data.

Low-resolution ($R \sim 5000$) spectropolarimetric observations were also collected with the FORS2 spectropolarimeter at the European Southern Observatories' (ESO) Very Large Telescope (VLT). Over six nights between 2010 February and May 2010, 48 exposures were collected, eight exposures per night, yielding six individual observations. The sequence of eight exposures were taken with the retarder plate positioned at angles of $-45°$, $-45°$, $+45°$, $+45°$, $-45°$, $-45°$, $+45°$, $+45°$ with respect to the axis of the Wollaston prism. The Stokes V parameter was extracted for each observation following the method of Bagnulo et al. (2002). A log of all our polarimetric observations is given in Table 1.

To increase the signal-to-noise ratio (SNR) of our ESPaDOnS spectra, we applied the Least-Squares Deconvolution (LSD) procedure of Donati et al. (1997) to all ESPaDOnS polarimetric data. As a starting point, our mask was based on a simple B2 star template containing only lines with intrinsic line depths greater than 10 per cent of the continuum. We then proceeded to remove all lines that were blended with hydrogen lines and any that were too weak to be visible in the spectrum of HR 5907 due to the high rotational broadening of the lines. What remained is a mask of 88 lines, most of which are helium lines. The resulting LSD profiles were computed on a spectral grid with a velocity bin of $9.0\,\mathrm{km\,s^{-1}}$, an example of which is shown in Fig. 1. The LSD method improved our sensitivity to weak Zeeman signatures by increasing the SNR by a factor of about 11 times compared to the peak SNR. We also list the improved LSD SNR measurements for each observation in Table 1. We find that each observation shows a clear Zeeman signature in the Stokes V profile and all but the profiles obtained on 2011 March 16 have a definite detection [false alarm probability (FAP) $<10^{-5}$] according to the criteria of Donati et al. (2002, 2006). The two profiles from this night have FAP of 1.677×10^{-3} and 7.744×10^{-3}. In no case do we detect a significant signal in the null profile for any of our extracted mean profiles (FAP $>10^{-3}$).

The longitudinal magnetic field (B_{ℓ}) and null measurements from the ESPaDOnS spectra were computed from each LSD Stokes V and diagnostic null profile in a manner similar to that described by Silvester et al. (2009), using an integration range from -400 to $400\,\mathrm{km\,s^{-1}}$. We find that the B_{ℓ} varies between -740 and -1845 G with a typical uncertainty of ~ 120 G. The longitudinal magnetic field was measured from the helium lines in the FORS data and were obtained in a manner similar to Rivinius et al. (2010) and Bagnulo et al. (2009, Appendix 2) using a χ^2 minimization technique. The uncertainties were computed following the method outlined by Rivinius et al. (2010) using a bootstrap Monte Carlo approach. We find a very similar range of values from -750 to -2048 G, but with typically larger uncertainties of ~ 250 G. The longitudinal field measurements from each polarimetric observation are also listed in Table 1.

2.2 Spectroscopy

A number of high-resolution spectra were acquired with the Ultraviolet and Visual Echelle Spectrograph (UVES) at the VLT. The

Table 1. Journal of polarimetric observations listing the date, the heliocentric Julian date (245 5000+), the number of sub-exposures and the exposure time per individual sub-exposure, the phase according to Equation 1, the peak SNR (per 1.8 and 3.4 km s^{-1} velocity bin in the ESPaDOnS spectra and FORS spectra, respectively) in the unpolarised spectra, the mean SNR per 9.0 km s^{-1} velocity bin in the LSD Stokes V profile, and the derived longitudinal field and longitudinal field detection significance z from both V and N. All ESPaDOnS observations, except the profiles obtained on 2011 March 16, have a definite detection of a signal in Stokes V (FAP $< 10^{-5}$) while no detection of a signal in the diagnostic null profile is found (FAP $> 10^{-3}$).

Date	HJD (2455000+)	t_{exp} (s)	Phase	Peak SNR	LSD SNR	V $B_\ell \pm \sigma_B$	z	N $B_\ell \pm \sigma_B$	z
				ESPaDOnS					
2010-02-24	252.0980	4 × 350	0.8244	1136	12786	−1573 ± 134	11.8	−111 ± 133	0.8
2010-02-24	252.1174	4 × 350	0.8626	1173	13318	−1201 ± 128	9.4	184 ± 128	1.4
2010-02-24	252.1358	4 × 350	0.8988	1285	14749	−1013 ± 115	8.8	−54 ± 115	0.5
2010-02-24	252.1541	4 × 350	0.9348	1177	13519	−1115 ± 125	8.9	101 ± 124	0.8
2010-02-24	252.1730	4 × 350	0.9719	1319	15138	−740 ± 110	6.7	94 ± 110	0.9
2010-02-25	253.0788	4 × 350	0.7542	1220	13993	−1686 ± 122	13.9	−1 ± 121	0.0
2010-02-25	253.0972	4 × 350	0.7902	1206	13839	−1733 ± 124	14.0	−141 ± 123	1.1
2010-02-25	253.1155	4 × 350	0.8262	1259	14474	−1554 ± 118	13.1	75 ± 118	0.6
2010-02-25	253.1338	4 × 350	0.8623	1218	13998	−1322 ± 122	10.8	−55 ± 122	0.5
2010-02-27	255.1211	4 × 350	0.7723	1217	13968	−1845 ± 123	15.0	−114 ± 123	0.9
2010-02-27	255.1395	4 × 350	0.8084	1216	13970	−1663 ± 123	13.5	−167 ± 123	1.4
2010-02-27	255.1579	4 × 350	0.8446	1234	14179	−1444 ± 121	11.9	55 ± 121	0.5
2010-02-27	255.1764	4 × 350	0.8810	1230	14139	−1301 ± 121	10.8	35 ± 120	0.3
2010-02-28	256.1063	4 × 350	0.7104	1265	14524	−1841 ± 119	15.4	−20 ± 119	0.2
2010-02-28	256.1246	4 × 350	0.7466	1165	13372	−1782 ± 128	13.9	42 ± 128	0.3
2010-03-03	259.1164	4 × 350	0.6328	1047	12010	−1709 ± 150	11.4	89 ± 150	0.6
2010-03-08	264.0532	4 × 350	0.3455	739	8442	−1708 ± 196	8.7	−296 ± 196	1.5
2010-03-08	264.1429	4 × 350	0.5221	1045	12003	−1821 ± 155	11.7	−31 ± 155	0.2
2010-07-23	400.7455	4 × 350	0.2786	1245	13727	−1665 ± 117	14.2	42 ± 116	0.4
2010-07-23	400.8317	4 × 350	0.4481	907	10089	−1708 ± 176	9.7	41 ± 175	0.2
2010-07-30	407.7708	4 × 350	0.1003	1213	13394	−1367 ± 122	11.2	14 ± 122	0.1
2011-02-19	612.1578	4 × 140	0.2183	748	8389	−1552 ± 186	8.3	1 ± 187	0.0
2011-02-19	612.1662	4 × 140	0.2348	831	9251	−1656 ± 171	9.7	33 ± 170	0.2
2011-03-12	632.9651	4 × 140	0.1554	698	7647	−980 ± 386	2.5	−3 ± 387	0.0
2011-03-12	632.9736	4 × 140	0.1720	778	8554	−1346 ± 189	7.1	−187 ± 188	1.0
2011-03-16	636.9714	4 × 140	0.0374	835	9205	−877 ± 182	4.8	172 ± 179	1.0
2011-03-16	636.9798	4 × 140	0.0539	764	8487	−852 ± 197	4.3	−98 ± 196	0.5
				FORS					
2010-03-30	285.6680	8 × 1.0	0.8712	915	–	−750 ± 251	3.0	441 ± 266	1.7
2010-04-18	304.7476	8 × 1.0	0.4091	879	–	−2330 ± 257	9.1	−46 ± 281	0.2
2010-04-20	306.8728	8 × 1.0	0.5903	1272	–	−1661 ± 218	7.6	−225 ± 184	1.2
2010-04-25	311.6637	8 × 1.0	0.0160	1187	–	−1389 ± 194	7.2	221 ± 180	1.2
2010-04-26	312.7446	8 × 1.0	0.1426	1076	–	−1739 ± 208	8.4	−207 ± 207	1.0
2010-05-04	320.6415	8 × 1.0	0.6793	993	–	−2048 ± 258	7.9	147 ± 199	0.7

instrument was used in its DIC2 437/760 setting giving us blue spectra from 375 to 498-nm and nearly continuous red spectra from 570 to 950 nm. A slit width of 0.8 arcsec was used resulting in a resolving power of $R = 50\,000$ over the entire spectrum. The details of these observations are listed in Table 2. In addition to the observations already described, archival *IUE* UV data obtained via the NASA-MAST archive were also used to constrain the fundamental parameters of HR 5907 (see Section 4). High-resolution and low-resolution observations exist in both the SWP and LWP spectral regions, both taken in large aperture mode. The high-resolution and low-resolution spectra are in good agreement, but we have only used the low-resolution spectra (both obtained on the night of 1989 July 26) here due to the higher SNR compared to the high-resolution spectra.

2.3 Photometry

Between 2011 April 15 and May 3 we obtained approximately uniform sampling of the photometric brightness variations of HR 5907

using the Microvariability and Oscillations of STars (MOST) satellite. The observations were obtained with the MOST satellite in switched-target mode, meaning that observations were scheduled such that multiple targets were observed during each MOST orbital period. During our observing run, half of the orbital phase was shared with observations of Arcturus. Each observation of HR 5907 consisted of 157 stacked 0.18-s exposures, resulting in a total of 9846 observations.

Photometric measurements of HR 5907 were obtained by performing aperture photometry on 20 × 20 pixel subrasters obtained from the MOST CCD photometer. We used a radius of 3 pixels for the photometric radius and a sky annulus of 8 pixels. Centroids were measured by fitting a Gaussian Point Spread Function (PSF). As with all MOST photometric studies, the raw photometry shows strong photometric variations correlated to the 101 min MOST orbital period. The variations are attributed to an increase in the measured background level of ∼200 ADU and to centroid shifts that map out intrapixel sensitivity changes across a CCD pixel. The photometric variations attributed to changes in the background level were measured to be ∼2 per cent and changes in centroid
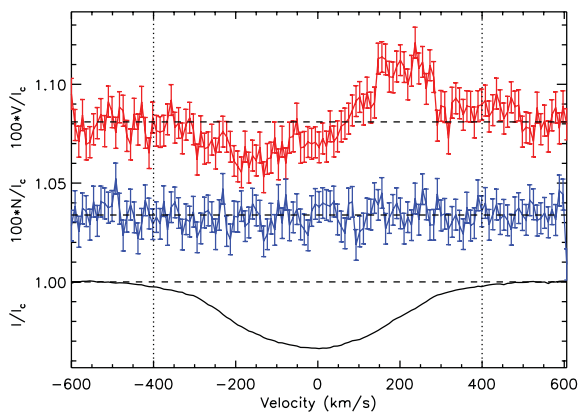
Figure 1. Mean LSD Stokes *V* (top), diagnostic null (middle) and Stokes *I* profiles (bottom) of HR 5907 from 2010 February 24. The *V* and *N* profiles are expanded by the indicated factor and shifted upwards for display purposes. A clear Zeeman signature is detected in the Stokes *V* profiles, while the null profile shows no signal. The error bars shown in the Stokes *V* and diagnostic null profiles represent the 1σ uncertainties. The integration limits used to measure the longitudinal field in the ESPaDOnS LSD profiles are indicated by the dotted lines.

position to be 0.3 per cent. HR 5907 also shows intrinsic periodic variations of ~4 per cent. In order to extract photometry free of instrumental effects a simultaneous fit was performed. The stray light was modelled with a third order polynomial, the intrapixel variations were modelled as a linear trend and intrinsic variations were modelled as a sinusoidal function with five additional harmonics. The fit was iterated after removing values of the centroid position
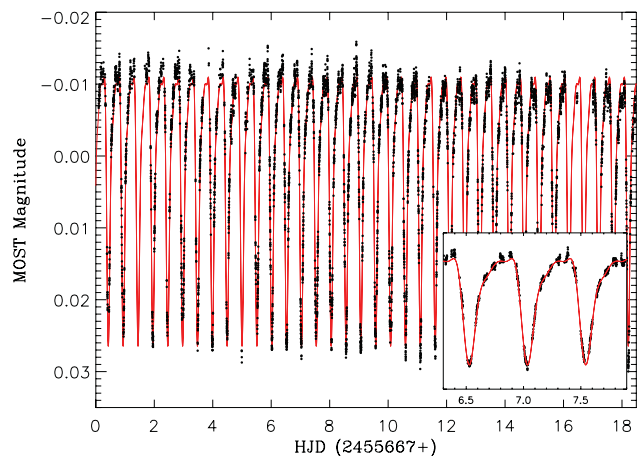

Figure 2. Brightness variations of HR 5907 as measured by the MOST satellite (black circles). The symbol size is chosen to represent the mean uncertainty of the data. The inset shows an expansion of the MOST data over a few nights to highlight the cycle to cycle variability and the clear periodicity. Also included is a red curve that corresponds to a best fit to the phased data (see Section 3 for further details).

and the full width half-maximum (FWHM) of the PSF beyond the 90 percentile. All data were excluded when the satellite passed through the South-Atlantic-Anomaly due to the large number of cosmic ray hits on the detector. The final reduced data set had an effective duty cycle of 26 per cent with 6062 photometric points.

The 18 d of observations cover roughly 36 cycles of the star, as illustrated in Fig. 2. These observations clearly demonstrate the

Table 2. Journal of UVES observations listing the date, the heliocentric Julian date (245 5000+), the exposure time, the phase according to Equation 1, and the peak SNR per 2.4 km s^{-1} velocity bin.

| Date	HJD (2455000+)	t_{exp} (s)	Phase	Peak SNR	Date	HJD (2455000+)	t_{exp} (s)	Phase	Peak SNR
	UVES 760L/760U					UVES 437			
2010-04-11	297.6922	12	0.5280	348 / 284	2010-04-11	297.6923	12	0.5281	444
2010-04-11	297.6939	18	0.5315	423 / 328	2010-04-11	297.6940	18	0.5315	488
2010-04-11	297.7972	18	0.7347	231 / 13	–	–	–	–	–
2010-04-11	297.7994	18	0.7389	446 / 329	2010-04-11	297.7995	18	0.7391	452
2010-04-11	297.9246	18	0.9852	349 / 295	2010-04-11	297.9246	18	0.9853	475
2010-04-12	298.6796	18	0.4706	345 / 383	2010-04-12	298.6796	18	0.4707	436
2010-04-12	298.6805	18	0.4725	310 / 321	2010-04-12	298.6806	18	0.4727	531
2010-04-13	299.6495	18	0.3789	511 / 318	2010-04-13	299.6495	18	0.3789	384
2010-04-13	299.6504	18	0.3807	384 / 274	2010-04-13	299.6505	18	0.3809	354
2010-04-13	299.7506	18	0.5777	373 / 283	2010-04-13	299.7506	18	0.5778	465
2010-04-13	299.7515	18	0.5795	395 / 422	2010-04-13	299.7516	18	0.5798	485
2010-04-13	299.8095	18	0.6937	447 / 312	2010-04-13	299.8096	18	0.6938	440
2010-04-13	299.8104	18	0.6954	389 / 304	2010-04-13	299.8104	18	0.6955	537
2010-04-13	299.9188	18	0.9088	263 / 216	2010-04-13	299.9189	18	0.9089	344
2010-04-13	299.9196	18	0.9103	343 / 281	2010-04-13	299.9196	18	0.9104	359
2010-04-13	299.9204	18	0.9119	269 / 209	2010-04-13	299.9204	18	0.9119	335
2010-04-13	299.9216	40	0.9142	451 / 304	2010-04-13	299.9216	40	0.9143	592
2010-04-13	299.9227	40	0.9163	405 / 291	2010-04-13	299.9227	40	0.9163	500
2010-04-13	299.9237	40	0.9183	399 / 260	2010-04-13	299.9237	40	0.9183	494
2010-04-13	299.9248	40	0.9205	507 / 310	2010-04-13	299.9248	40	0.9206	491
2010-04-13	299.9258	40	0.9225	494 / 290	2010-04-13	299.9258	40	0.9226	489
2010-04-13	299.9268	40	0.9245	477 / 314	2010-04-13	299.9266	40	0.9246	490
2010-05-30	346.7541	18	0.0540	281 / 186	2010-05-30	346.7542	18	0.0542	290
2010-05-30	346.8314	18	0.2061	221 / 183	2010-05-30	346.8314	18	0.2062	271
2010-05-30	346.8322	18	0.2077	255 / 185	2010-05-30	346.8322	18	0.2077	230
2010-05-30	346.8330	18	0.2092	291 / 161	2010-05-30	346.8330	18	0.2092	215
2010-06-08	356.4791	18	0.1873	465 / 224	2010-06-08	356.4791	18	0.1874	328
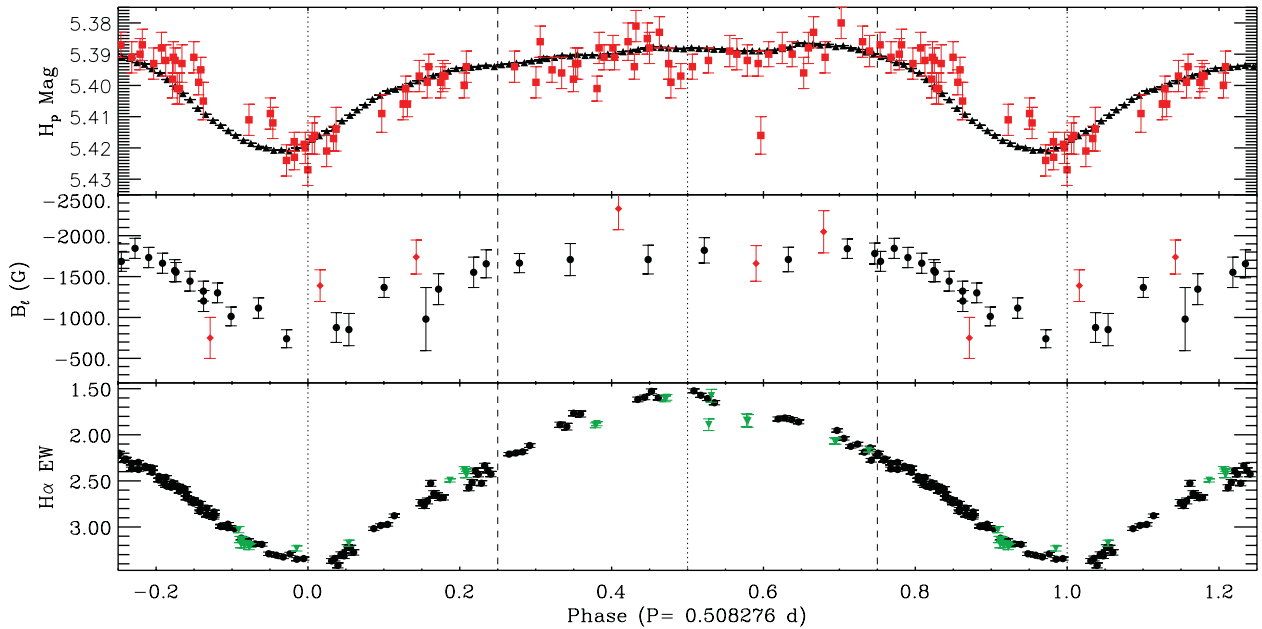
Figure 3. Phased observational data according to ephemeris given in equation (1): Upper panel: MOST (black triangles) and *Hipparcos* (red squares) photometry. The MOST data have been binned in 0.01 phase bins and shifted to the *Hipparcos* magnitude for display purposes. Middle panel: longitudinal magnetic field variations measured from ESPaDOnS (black circles) and FORS (red diamonds) data. Lower panel: Hα EW variations measured from ESPaDOnS (black circles) and UVES (green triangles). We have also drawn dotted lines indicating phases 0.0 and 0.5, and dashed lines indicating phases 0.25 and 0.75.

approximately 0.5-d rotational cycle (see Section 3 and Fig. 3 for further details). Also shown in Fig. 2 is an expansion of a few cycles that emphasizes the non-sinusoidal, but periodic brightness variations. The sharpness of the photometric minimum is not consistent with brightness patches or other surface features and requires a structure that is geometrically thin, likely of circumstellar origin. We note that the observed photometric variations are consistent from cycle to cycle, but that there are additional small intrinsic variations beyond the expected scatter about the uncertainty, which cannot be attributed to any instrumental or orbital effects.

3 EPHEMERIS

HR 5907 was first identified as a photometric variable star with a period of 0.508 d based on *Hipparcos* data (Hubert & Floquet 1998). Lefèvre et al. (2009) later confirmed this variability but adopted a period that was twice as long (1.017 d), since they assumed it was due to binary effects. We re-analysed the *Hipparcos* data set using a Lomb–Scargle like technique (Press et al. 1992) and confirm a best-fitting period of 0.508 31 ± 0.000 03 d. We also confirm that the current epoch of longitudinal magnetic field measurements, Hα equivalent width (EW) variations (see Section 5) and MOST photometry phase well with this period. However, because of the long baseline between the *Hipparcos* era photometry and the current MOST photometry, choosing any period within the uncertainty range can lead to a phase shift between the phased *Hipparcos* and MOST photometry of upwards of 0.5 cycles. Unfortunately, as the MOST data only covers about 36 rotation cycles, we cannot obtain a more precise period from this data set. Applying the Lomb–Scargle-like technique to our extensive Hα EW data set does provide a more precise period of 0.508 25 ± 0.000 01 d, but this period is inconsistent with the *Hipparcos* period. In either case, we believe that the periodic variations are sufficiently non-sinusoidal that the Lomb–Scargle technique is inadequate.

We proceeded by adopting a multiharmonic fitting technique similar to Schwarzenberg-Czerny (1996), which is ideal for non-sinusoidal periodic variations. After including contributions from the first three harmonics to both the Hα EW variations and the *Hipparcos* photometry we find a best-fitting period of $0.508\,274^{+0.000\,010}_{-0.000\,012}$ d from the EW variations and a best-fitting period of $0.508\,276^{+0.000\,015}_{-0.000\,012}$ d from the *Hipparcos* photometry. A similar analysis of the MOST data results in a best-fitting period of $0.508\,269^{+0.000\,021}_{-0.000\,040}$ d period. The uncertainties on these newly derived periods are still large enough that the phasing uncertainty between the *Hipparcos*-era and current epoch of data is not resolved. In any event, we adopt the *Hipparcos* period as it provides good agreement between the *Hipparcos* and MOST photometry, as is expected unless significant rotational braking has occurred (see Section 8 for further details). Therefore, within the context of an oblique rotator model, we adopt this period as the rotational period of HR 5907, which results in this star having the shortest known rotational period of any non-degenerate, magnetic massive star. Taking the Hα EW maximum as T_0 we derive the following ephemeris:

$$\text{HJD}^{\text{max}}_{\text{H}\alpha} = 2447913.694(1) + 0.508276(^{+15}_{-12})E, \qquad (1)$$

where the uncertainties in the last digits are indicated in brackets. Unless otherwise stated, all further data are phased according to this ephemeris.

4 FUNDAMENTAL PARAMETERS

In order to investigate the fundamental parameters of HR 5907 we utilized the third revision of the BRUCE and KYLIE software suite (hereafter referred to as BK3; Townsend 1997). While BK3 is capable of producing theoretical spectra in both absolute flux and continuum normalized flux from either ATLAS9 LTE atmospheres (Kurucz 1992) or from NLTE TLUSTY atmospheres of Lanz & Hubeny (2007), only solar abundance LTE atmospheres were used
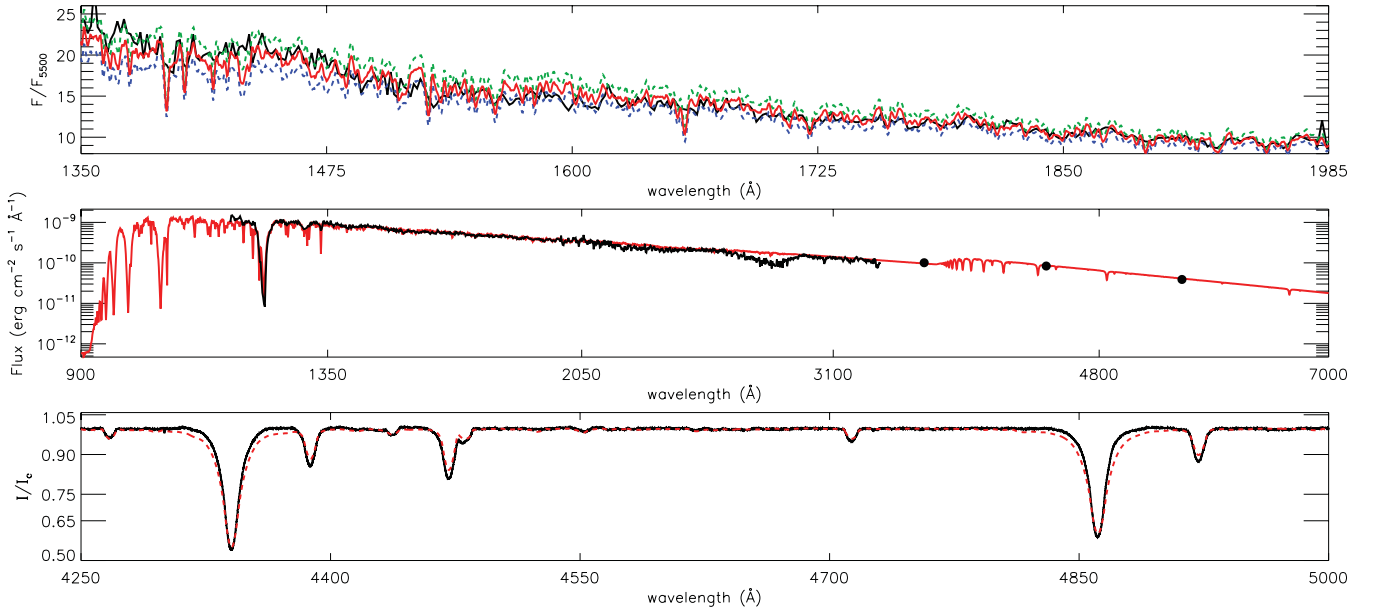
Figure 4. Comparison between BK3 model and observed data: Upper panel: *IUE* UV spectrum normalized to flux at 5500 Å and best-fitting model with $T_{\rm eff}$ of 17 000 K (red) along with models corresponding to 16000/18000 K (blue/green). Middle panel: *IUE* UV SED and Johnson *UBV* photometry (black) with best overall global model with $T_{\rm eff} = 17\,000$ K, $M_\star = 5.5\,{\rm M}_\odot$, $R_{\rm eq} = 3.1\,{\rm R}_\odot$ and an inclination of $i = 70°$. Bottom panel: ESPaDOnS normalized spectrum (corresponding to observation with the least emission (24 February 2010; black)) with best-fitting overall model (red). Note that the poor fit to the Balmer wings (bottom panel) is likely due to the over-normalisation of the ESPaDOnS spectrum.

in this study. This was decided due to the fact that we found a much better overall agreement between the line strengths of C II and Si II lines in the blue region with solar abundance LTE atmospheres in comparison to solar abundance NLTE atmospheres. In our analysis, both the observed spectra and synthetic spectra were renormalized to the continuum regions surrounding the individual line profiles before the comparisons.

In the following discussion, we assume that modelling a rapidly rotating star depends on five independent parameters, which we choose to be the equatorial velocity $v_{\rm eq} \sin i$, the inclination angle of the rotation axis relative to the line-of-sight i, the effective temperature $T_{\rm eff}$, the stellar mass $M_\star$, and the stellar equatorial radius $R_{\rm eq}$. As input, BK3 uses our estimated period $P = 0.508\,276$ d to constrain the equatorial values for relevant parameters. In order to determine the properties of HR 5907, we searched through a grid of models that varied the previously listed fundamental parameters for a fixed P.

4.1 Effective temperature

Our primary method to constrain the $T_{\rm eff}$ of HR 5907 was from a dereddened spectral energy distribution (SED). We note that BK3 uses $T_{\rm eff}$ in the sense that it is the solid angle integrated, uniform blackbody temperature that a star of the same surface area would need to have, such that the total luminosity is the same as the actual gravity darkened star. In this context, BK3 allows for different local temperatures over the surface of the star.

We constructed an SED for HR 5907 by combining the *IUE* UV data with flux calibrated *UBV* photometry (Jaschek & Egret 1982; Kharchenko & Roeser 2009), using calibrations of Hynes (2011). To deredden our spectra we adopted a $(B - V)_0 = -0.18$ corresponding to a temperature between 17 and 18 kK. This temperature, as suggested by our initial fits to the C II 4267 Å line, is cooler than otherwise suggested by HR 5907's B2.5 spectral

classification. However, based on our initial temperature fits and the stronger than predicted helium absorption lines, HR 5907 may in fact be a He-strong star and therefore the cooler temperature is justified. With this $(B - V)_0$ we find that $E(B - V) = 0.14$, which is slightly lower than the value determined by Papaj, Wegner & Krelowski (1991) ($E(B - V) = 0.155$) who adopted a standard B2 star template for their analysis. We do not find any significant differences in our results if we adopt this slightly higher value.

The SED was then extinction corrected using the parametric law of Cardelli, Clayton & Mathis (1989), with $R_V = 3.1$, and we then normalized the SED by the flux at 5500 Å so that we could constrain the temperature by fitting the slope of the UV spectrum, removing the need for any distance or luminosity corrections. As illustrated in the top panel of Fig. 4, we find a best-fitting $T_{\rm eff} = 17\,000 \pm 1000$ K when fitting the 1250–2000 Å range of the SED. We note that if we adopt an $R_V = 3.9$ as found by Lewis et al. (2009), we find a slightly cooler temperature of 16 500 K, but still within our uncertainty. We also confirm that adopting a NLTE model atmosphere results in a best-fitting $T_{\rm eff}$ within our uncertainty.

4.2 Projected rotational velocity and radius

As previously mentioned, we could also independently constrain the $T_{\rm eff}$ by fitting the line depth of the C II 4267 Å line profile, as i or $M_\star$ has very little affect on the shape of this line and it only varies slightly with $R_{\rm eq}$. However, there is still a strong dependence of the line depth from the rotational broadening.

We simultaneously fit the $T_{\rm eff}$ and the projected rotational velocity $v_{\rm eq} \sin i$ of the star by searching for the model that provided the best overall fit to the C II profile. We first constructed a mean profile from all of our ESPaDOnS spectra before comparing this profile to our grid of models. The ESPaDOnS profile was best fitted by a model with $T_{\rm eff} = 17\,000 \pm 1000$ K and $v_{eq} \sin i = 290 \pm 10$ km s^{-1}.
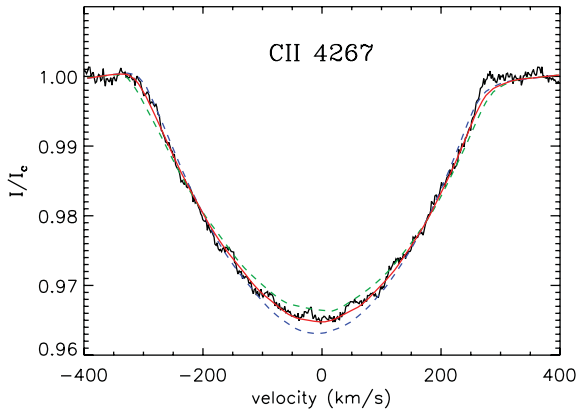
Figure 5. Comparison between the mean profile from ESPaDOnS data (black) and best-fitting model with $T_{\rm eff} = 17000$ K, $v\sin i = 290$ km s^{-1} (red) and $v\sin i = 280$ and 300 km s^{-1} (dashed blue and green, respectively).

Figure 6. Left panel: Hertzsprung-Russell diagram showing the position of HR 5907 as found in this work (black square) and as found by Hernández et al. (2005) (red circle). Also shown are stellar evolutionary tracks (dashed) and the zero-age main sequence (solid) from Bertelli et al. (2009). Right panel: Comparison of our best-fitting model ($T_{\rm eff} = 17$ kK, $M_\star = 5.5$ M$_\odot$, $R_{eq} = 3.1$ R$_\odot$) with the FORS observation from 25 April 2011 showing the least emission, for the Hδ region.

As a check, we also compared our models with a mean profile constructed from the UVES data that resulted in a best-fitting $T_{\rm eff} = 17\,000$ K, and a slightly lower $v_{\rm eq}\sin i = 285$ km s^{-1}, which is still consistent with our findings from the ESPaDOnS spectra. We adopt $v_{\rm eq}\sin i = 290 \pm 10$ km s^{-1} since our mean ESPaDOnS profile is constructed from a set of observations that better span the entire rotational cycle. A comparison between our best-fitting model and our mean ESPaDOnS profile is shown in Fig. 5. By combining our best-fitting $v_{\rm eq}\sin i$ and rotational period P, we find that $R_{\star,\rm eq}\sin i \sim 2.91$ R$_\odot$.

4.3 Stellar mass and inclination

With $v_{\rm eq}\sin i$ and $T_{\rm eff}$ determined, the remaining unknown model parameters are $M_\star$ and i, since $R_{\rm eq}$ is constrained by P and $v_{\rm eq}\sin i$. To infer the mass of HR 5907 we made use of the revised parallax from the *Hipparcos* catalogue ($\pi = 7.64 \pm 0.37$; van Leeuwen 2007) to obtain the absolute magnitude M_V and therefore obtain HR 5907's placement on a Hertzsprung–Russell (HR) diagram. The visual extinction A_V and magnitude V were taken to be 0.43 (this work) and 5.4 (Kharchenko & Roeser 2009), respectively. Using a bolometric correction corresponding to $T_{\rm eff}$ from our model ($BC = -1.6 \pm 0.2$; Lanz & Hubeny 2007) we computed the bolometric magnitude ($M_{\rm BOL} = M_V + BC$) and finally the luminosity $L_\star$. Our final luminosity is found to be $\log (L_\star/L_\odot) = 2.78 \pm 0.14$ (using the absolute bolometric corrected solar magnitude M$_\odot$ = 4.74), with the uncertainty found through propagation of the uncertainty in the distance and the bolometric correction.

As shown in Fig. 6, we compared HR 5907's placement with available Padova evolutionary tracks ($Y = 0.26$; Bertelli et al. 2009) and find that HR 5907 has a mass of $\sim$5.2 M$_\odot$. Also included in Fig. 6 are the results of Hernández et al. (2005) who find HR 5907 slightly hotter and more luminous, but still consistent with our findings. The Padova evolutionary tracks may lack any effects due to rotation, but according to the work of Maeder & Meynet (2010), the inclusion of rotation would shift the evolutionary track such that a star of a particular mass and age would be slightly cooler and slightly brighter when rotation is included. Therefore, if we used tracks that included rotation, then based on HR 5907's position we would only expect to find small changes (within our uncertainty) that would result in this star being slightly closer to the main sequence and having a slightly higher mass.
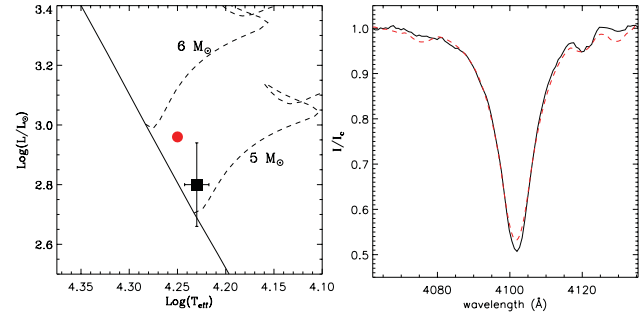
We can also constrain the mass and inclination from fits to the Balmer wings, which are sensitive to surface gravity ($g = G\,M_\star/R_\star^2$). Unfortunately, this can be quite problematic with HR 5907 as there is considerable emission in the wings of the Balmer lines due to circumstellar plasma (see Section 7). However, we still proceeded by using the FORS spectrum from 2011 April 25 that showed the least emission in the Balmer wings. The long-slit FORS spectra are ideal since they are less susceptible to the over-normalization of the Balmer lines that can occur with the multi-order ESPaDOnS and UVES spectra. We proceeded by searching for the model (at a fixed $T_{\rm eff}$, but varying mass and radius) that provided the best fit to the wings of the Hδ line profile, since lower Balmer series lines are more affected by the circumstellar plasma, and higher Balmer series lines were more difficult to ensure consistent normalization between the model and observed spectrum. An overall best-fitting model was found with $M_\star = 5.5 \pm 0.5$ M$_\odot$ and $R_{\rm eq} = 3.1 \pm 0.1$ R$_\odot$ (a comparison is shown in the right-hand panel of Fig. 6), consistent with the mass estimates derived from HR 5907's placement on the HR diagram. If we adopt $M_\star = 5.5 \pm 0.5$ M$_\odot$ and $R_{\rm eq} = 3.1 \pm 0.1$ R$_\odot$ this implies that values of $i = 70^{+20°}_{-10}$ are allowed.

Independently, we can also use the BK3 models to fit the absolute, extinction-corrected SED of HR 5907. Using the previously stated parallax value, we first corrected the SED to an absolute distance consistent with the BK3 models. We then proceeded by fitting the *IUE* UV spectra (between 1250 and 2000 Å) with the BK3 models. From this method we also find a best-fitting $R_{\rm eq} = 3.1 \pm 0.1$ R$_\odot$ and $i = 70 \pm 10°$ for masses around 5 M$_\odot$, as shown in the middle panel of Fig. 4. However, if we use the R_V value of Lewis et al. (2009) and the slightly cooler temperature that results from those fits, we would find a slightly smaller equatorial radius of 2.9 R$_\odot$. We therefore adopt a slightly higher uncertainty of 0.2 R$_\odot$. A summary of the fundamental stellar parameters is listed in Section 8. A comparison between our best-fitting model and the ESPaDOnS spectrum with the lowest emission is included in the bottom panel of Fig. 4.

5 LINE VARIABILITY

Because of HR 5907's rapid rotation and the need to sample fast photospheric variations, we opted to use the individual sub-exposures that make up the polarimetric ESPaDOnS observations for all our line profile variability analysis. The individual sub-exposures are still of sufficient quality, with SNRs comparable to the UVES data.

To begin, we can characterize the variability from variations in the EWs of the spectral lines. Before measuring the EW, each spectral line was renormalized to the surrounding continuum, and a telluric correction algorithm was applied to regions redward of 5790 Å. The EWs were then obtained by numerically integrating over the line profile. The 1σ uncertainties were computed by adding the individual pixel uncertainties in quadrature. For the UVES data, a single uncertainty value was assigned to each pixel, determined from the RMS scatter in the continuum regions surrounding the line profile. The EW variations for a number of spectral lines were measured and then phased with the ephemeris given in Equation 1, with the results presented in Figs 3, 7 and 8. We find small systematic offsets between the UVES data and the ESPaDOnS data on the order 0.01 Å for most helium and metallic lines. However, a larger offset

is found in the broader Balmer and Pashen lines. We do not find any significant differences in the morphology of the line profiles between the two data sets at the same phase, but we do find weak but wide-scale systematic differences. We attribute these systematic offsets to inconsistencies in the normalization between the two data sets, which is common due to complexity of extraction and normalization of echelle spectra. Therefore, the UVES EW values have all been corrected to best match the ESPaDOnS measurements by subtracting fixed offsets between the two data sets.

As depicted in Fig. 7, helium lines show obvious EW variations, consistent with the rotational period, as measured from our high-resolution spectra. The observed EW variations do not vary in a similar manner to the circumstellar Hα variations depicted in Fig. 3 and we speculate that they are due to photospheric abundance
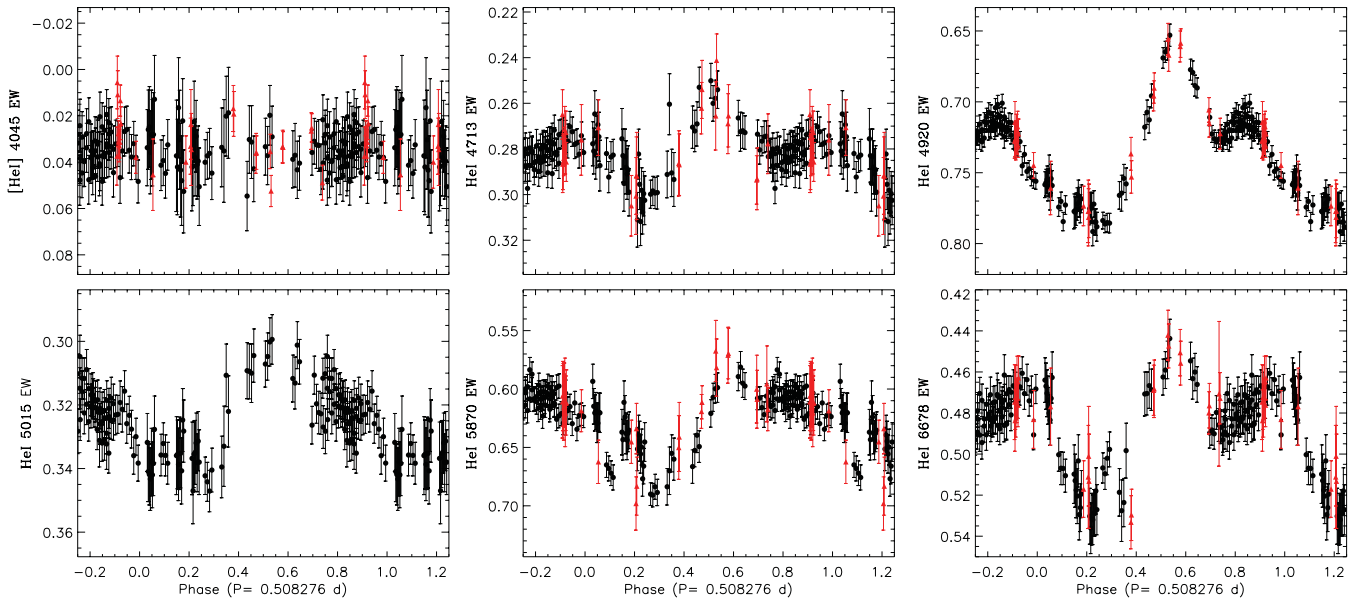

Figure 7. Phased EW variations of selected helium lines in the spectrum of HR 5907, measured from ESPaDOnS (black circles) and UVES (red triangles) data.
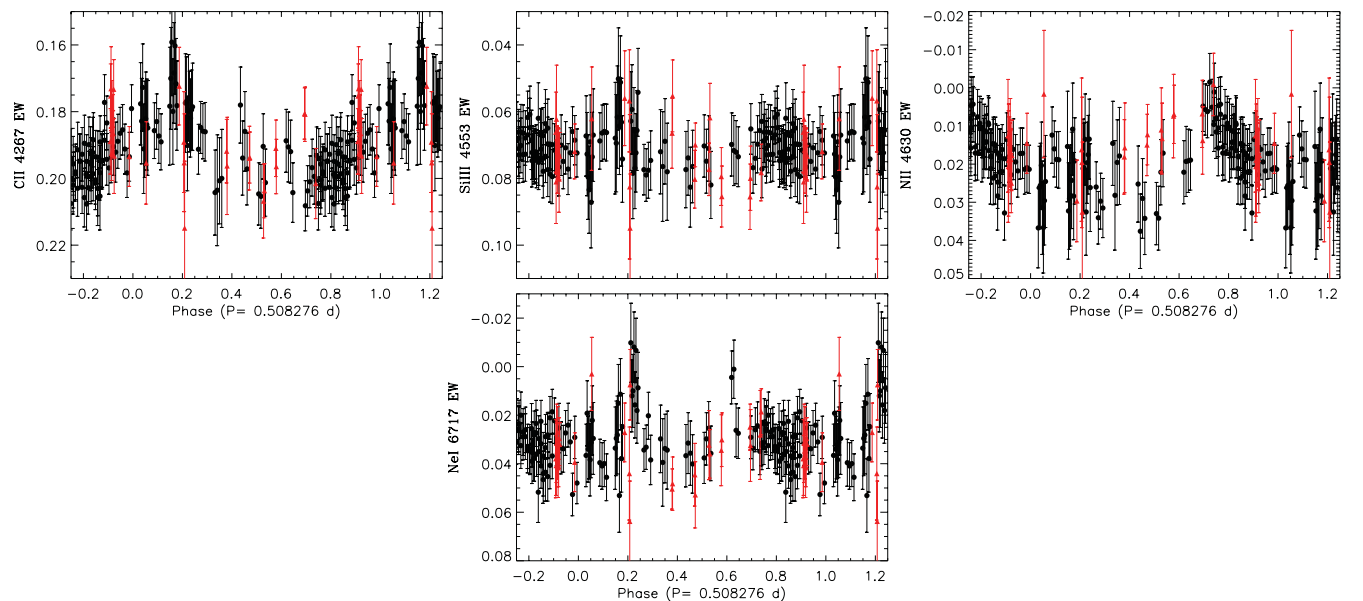

Figure 8. Phased EW variations of selected metal lines in the spectrum of HR 5907, measured from ESPaDOnS (black) and UVES (red) data.
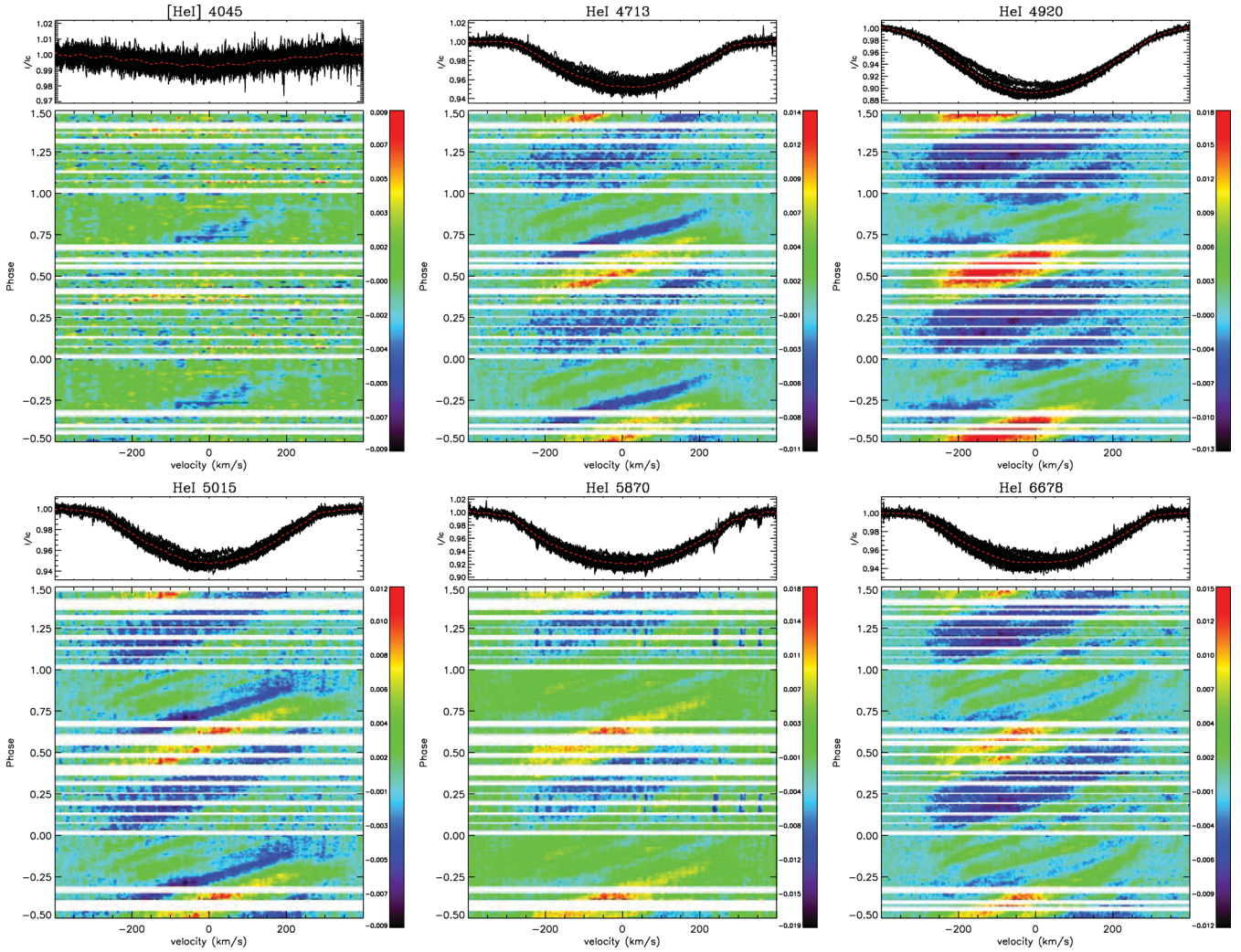
Figure 9. Phased variations of photospheric helium lines.

patches, consistent with findings from investigations of other He-strong/variable stars (e.g. Bohlender & Landstreet 1988).

The clearest variability is seen in the He I 4920 Å line, which reaches maximum absorption (corresponding to a minimum EW in Fig. 7) around phase 0.25 and minimum absorption around phase 0.55. Another local minimum is found around phase 0.85, indicating a relatively complex helium abundance pattern in the photosphere of HR 5907. In contrast to the large EW variations seen in He I 4920 Å, very little variability is observed in the forbidden [He I] 4045 Å line. In the other helium lines shown in Fig. 7, we see a variability pattern similar to the 4920 Å line, but with a smaller amplitude. In comparison to other He-strong stars such as σ Ori E (e.g. Landstreet & Borra 1978; Reiners et al. 2000; Smith & Bohlender 2007) or HR 7355 (Rivinius et al. 2010) we find that HR 5907 shows relatively weak variability in its helium lines, of ∼20 per cent in EW.

We also investigated the EW variability of a number of other photospheric absorption lines, the results of which are displayed in Fig. 8. In comparison to the helium lines, very little variability is seen in these lines. Only the lines of carbon and nitrogen, as evidenced in Fig. 8 (top left and top right panels) show any obvious signs of periodic variations. The EW curve for carbon is approxi-

mately sinusoidal, with maximum absorption around phase 0.2 and minimum absorption at about phase 0.7. The nitrogen EW curve is also simple, but appears to be a non-sinusoidal variation.

We can further investigate the photospheric variations by examining the phased intensity variations of these line profiles, commonly referred to as 'dynamic spectra', as shown in Figs 9 and 10. In these figures, individual spectra are represented as horizontal bands with intensity encoded by different colours and are stacked vertically according to their phase to illustrate time variability. To further highlight these variations, we have also subtracted from each profile the mean spectrum formed by averaging all the profiles.

The dynamic spectrum of the [He I] 4045 Å line (Fig. 9 upper left panel) shows a very weak but simple pattern with one clear enhanced absorption feature travelling from negative to positive velocities, crossing $v_{sys} = 0 \, \mathrm{km \, s^{-1}}$ at about phase 0.75 (where v_{sys} represents the systemic velocity of HR 5907). The absorption feature is likely a region of the stellar photosphere where helium is found to be overabundant compared to the mean helium surface distribution. This feature is also present in all the other helium lines shown in Fig. 9, but appears to be the less prominent absorption feature in the other helium lines. A significantly larger and more absorptive feature is found to cross $v_{sys} = 0 \, \mathrm{km \, s^{-1}}$ at about phase 0.25 in
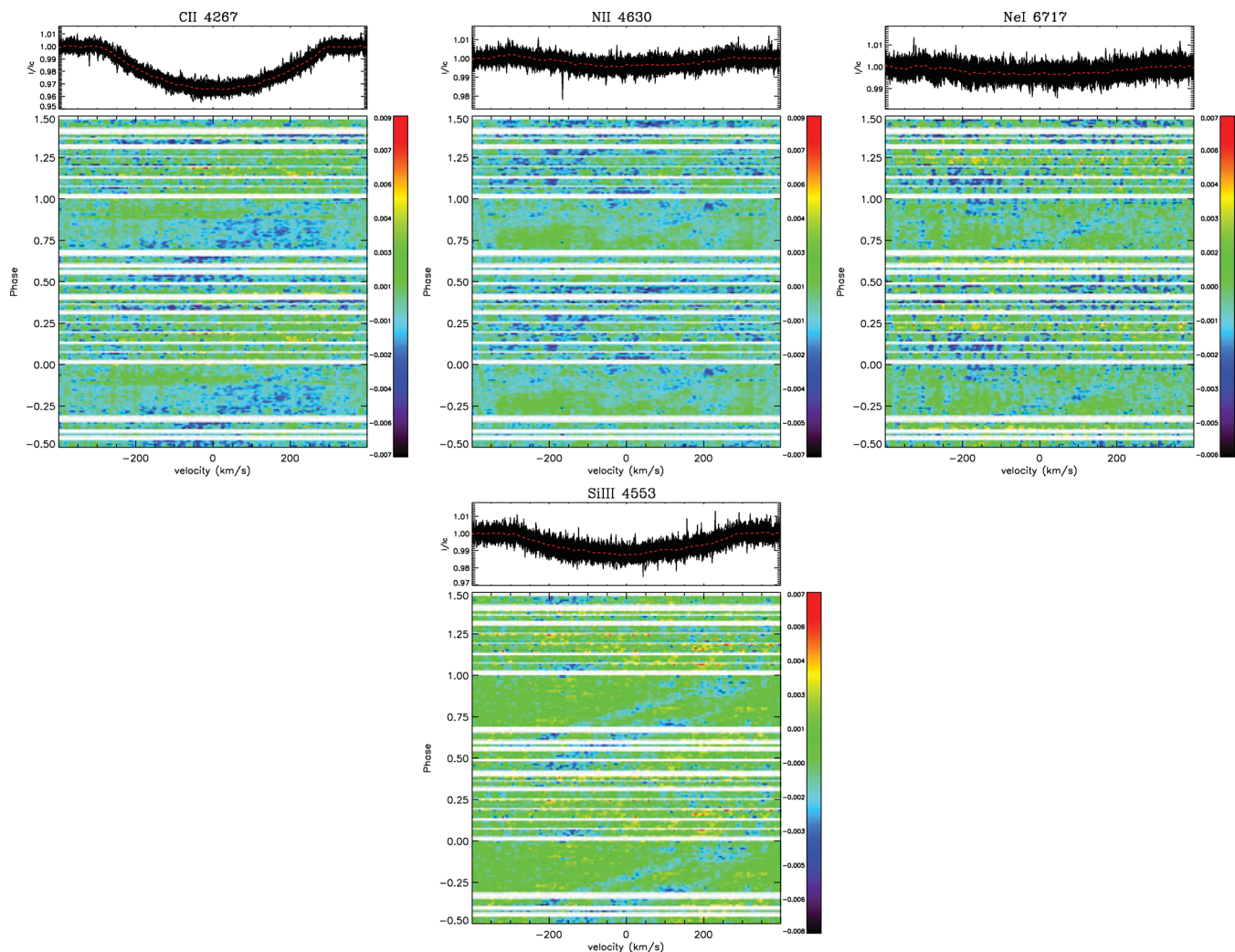
Figure 10. Phased variations of selected metallic photospheric lines.

all the other helium lines. Additionally, these stronger helium lines also show a clearly more complex dynamic spectrum. In these lines there also appears to be the presence of a strong pseudo-emission feature (this feature only appears in emission relative to the mean profile and represents a region of the stellar photosphere where helium is underabundant with respect to the mean helium surface distribution), which crosses $v_{sys} = 0\,\mathrm{km\,s^{-1}}$ around phase 0.6. In some of the lines (e.g. He I 4713, 5015 and 6678 Å) additional pseudo-emission features can be found with one crossing $v_{sys} = 0\,\mathrm{km\,s^{-1}}$ around phase 0.8 and the other around phase 0.0. These two features are much narrower than the feature that crosses at phase 0.6, and do not reach the same intensity of pseudo-emission.

If we look at the dynamic spectra of the metallic lines (Fig. 10), we find a single extremely weak pseudo-emission feature that crosses $v_{sys} = 0\,\mathrm{km\,s^{-1}}$ around phase 0.2 in C II or an enhanced absorption feature crossing $v_{sys} = 0\,\mathrm{km\,s^{-1}}$ around phase 0.6 (upper left panel). We have also tentatively identified a weak absorption feature in N II and Ne I crossing $v_{sys} = 0\,\mathrm{km\,s^{-1}}$ around phase 0.2, which appears to be in antiphase with the absorption feature found in the C II line. However, these lines are very weak, making it difficult to distinguish any features relative to the noise level. In the dynamic spectrum of Si III 4553 Å (bottom panel), we find two absorption features closely spaced in phase, with one crossing $v_{sys} = 0\,\mathrm{km\,s^{-1}}$ around phase

0.65 and the other crossing around phase 0.8. These variations appear to be in phase with the C II variations.

6 MAGNETIC FIELD GEOMETRY

To investigate the magnetic field geometry of HR 5907 we assume that the field can be described by the dipole Oblique Rotator Model (ORM). This model is characterized by four parameters: the phase of closest approach of the magnetic pole to the line of sight ϕ_0, the inclination of the stellar rotation axis i, the obliquity angle between the magnetic axis and the rotation axis β and the dipole polar strength B_d. Our first approach was to model the longitudinal field curve, as shown in Fig. 3. This was carried out using a χ^2 minimization to compare the observed longitudinal field curve to a grid of computed longitudinal field curves to determine B_d and β. For this analysis we have assumed $i = 70°$ (as determined in Section 4.3) and a limb darkening coefficient of 0.4.

The resulting χ^2 landscape from our fits is shown in Fig. 11. Our results indicate that we are viewing the negative (southern) hemisphere of the magnetic field and that HR 5907 hosts a field with a polar surface strength of $B_d = 15700^{+800}_{-900}$ G, an obliquity angle of $\beta = 7^{+1\,\circ}_{-2}$ and that $\phi_0 = 0.48$. Despite relatively small formal uncertainties our best-fitting model is not capable of fitting
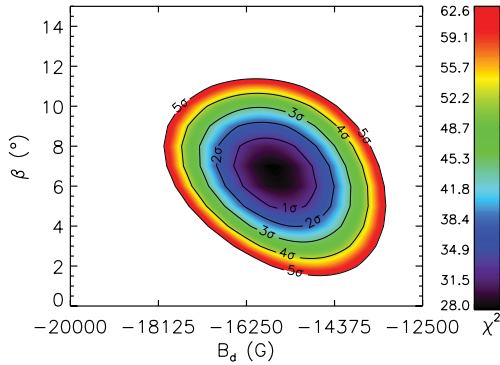
Figure 11. χ^2 landscape of dipole field strength B_d versus magnetic obliquity β permitted by the longitudinal field variation of HR 5907, assuming $i = 70°$.
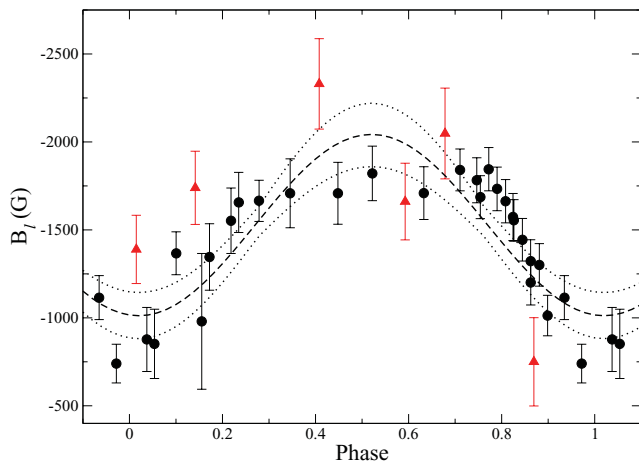

Figure 12. Longitudinal field variations of HR 5907 from ESPaDOnS (black circles) and FORS (red triangles) compared to our best-fitting model curve (dashed) with $B_d = 15700$ G and $\beta = 7°$. The dotted lines indicated the 1σ limits permitted by our fits.

the measured longitudinal field measurements at each phase, as illustrated in Fig. 12, and as indicated by the best-fitting reduced $\chi^2 = 2.0$ from the FORS and ESPaDOnS data sets combined, or 2.1 from ESPaDOnS data alone.

Still within the framework of the ORM, our second procedure compares the observed mean LSD Stokes V profiles to a large grid of synthetic profiles that are parametrized by B_d, β, the phase ϕ and i. The models are computed by performing a disc integration of local Stokes V profiles assuming the weak field approximation and a uniform surface abundance. The parameters of the Stokes V profiles were chosen to fit the mean LSD Stokes I profile created from the average of all our observations. We adopted the ϕ_0 we obtained from our longitudinal field curve fits, but find that the derived value of β does not vary much for small changes in ϕ_0 and that the derived values of B_d only vary by a few hundred gauss. For each Stokes V profile we found the parameters that provided the lowest χ^2 for each observation. Using a Bayesian framework, we then combined the χ^2 distributions obtained for each observation to find the maximum likelihood model. In Fig. 13 we compare the synthetic profiles of our maximum likelihood model (dotted red) with the best-fitting model for each observation (dashed blue). The quality of the fits are similar, showing that a single dipole configuration can, for most phases, roughly reproduce the observed mean profiles. However, as

with our fits to the longitudinal field curve, some phases are rather poorly fit by the ORM model.

The maximum likelihood model was found with $B_d = 10400^{+280}_{-350}$ G and $\beta = 7 \pm 1°$, where the uncertainties represent the 95 percentile range. While the formal uncertainties are quite low, we note that the individual best fits to each observation have best-fitting parameters ranging from $B_d \sim 4000$–25000 G and $\beta \sim 0$–15°.

Therefore, modelling of the longitudinal field curve and Stokes V profiles indicate a strong magnetic field nearly aligned with the rotation axis. However, the observations at different phases differ quite significantly from the overall best-fitting model. This will be further discussed in Section 8.

7 THE MAGNETOSPHERE

Within the context of the magnetosphere model, the common picture is that the variability that is observed in hydrogen lines among Bp stars results from the circumstellar plasma. This plasma is centrifugally supported and magnetically confined into clouds that are forced into co-rotation with the host star (e.g. Shore & Brown 1990; Shore et al. 1990; Shore 1993; Townsend & Owocki 2005; ud-Doula, Owocki & Townsend 2008). The circumstellar gas is seen in emission (usually in hydrogen and a few other lines) at quadrature phases, and in absorption when passing in front of the star.

As with the photospheric variability, we begin by first analysing the EW variations in the hydrogen Paschen and Balmer lines. As discussed in Section 3, HR 5907 shows strong EW variations due to the circumstellar emission in Hα. In Fig. 14 the EW variations for a number of Paschen and Balmer lines are also depicted. The strongest variation and simplest pattern is that of Hα (Fig. 14 bottom left-hand panel and Fig. 3 bottom panel), which shows a single emission peak at phase 0.5. This basic pattern is also present in the higher Balmer lines such as Hβ and Hγ (Fig. 14 bottom panels), but with much more noise. However, there also appears to be a second, smaller absorption dip in the Hβ EW variations at phase 0.6 that is not present in the other Balmer EW variations. If we now look at the Paschen lines, which probe the magnetosphere at a different optical depth (Fig. 14 top panels), we see a much more complex EW curve, composed of many smaller local absorption dips in addition to the single large emission peak. The overall structure of the EW curve for the Paschen lines is similar, but the amplitude of the local absorption variability varies significantly among the different lines available in the ESPaDOnS/UVES spectral range. We find the Pa$_{15}$ line to show the strongest overall variability, but Pa$_{14}$ has less scatter in the EW variations showing a local maximum emission at phase 0.18, followed by a local minimum emission at phase 0.33. Another local maximum in the emission is found at phase 0.69, but there also appears to be some additional structure to the EW curve between phases 0.33 and 0.69 that is poorly sampled by our data.

We can further our understanding of the magnetospheric structure by studying the dynamic spectra shown in Figs 15 and 16. However, unlike the dynamic spectra shown in Section 5, these dynamic spectra only include contributions from the emission, as a theoretical photospheric profile has been subtracted from each observation. In Fig. 15, we subtracted profiles corresponding to the best-fitting BK3 model determined in Section 4. Since these models do not extend into the Paschen region, we found the TLUSTY model (Lanz & Hubeny 2007) that provided the best fit to the Balmer lines of our BK3 model. This best-fitting model ($T_{\rm eff} = 19$ kK and $\log(g) = 4.25$) was found to reproduce the wings of the BK3 model Balmer lines well, but has a core that is less deep than the same BK3 model.
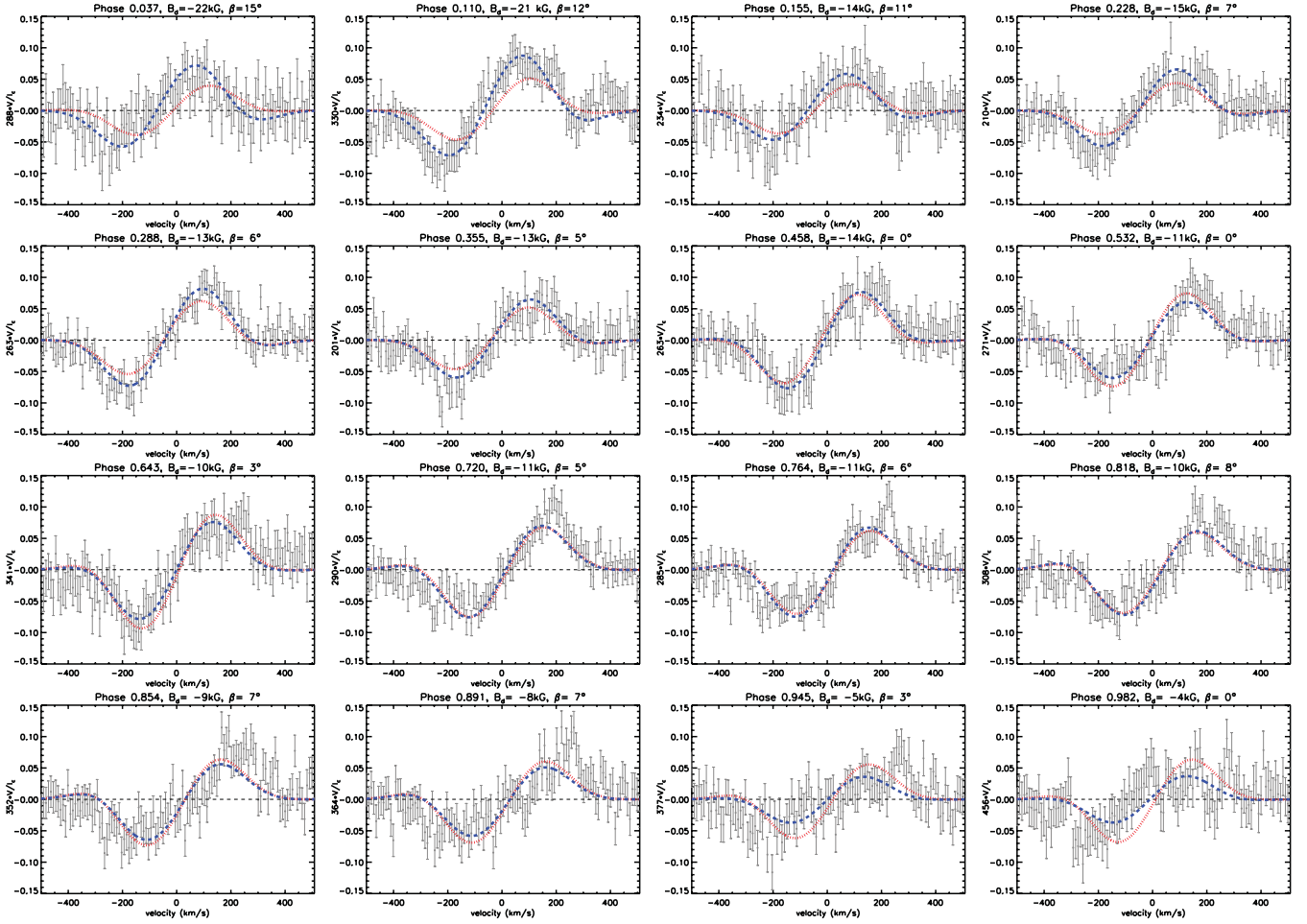
Figure 13. Selected mean circularly polarized LSD Stokes *V* profiles (grey circles) obtained from the ESPaDOnS data set sampling the rotational cycle of HR 5907. The error bars represent the 1σ uncertainties for each pixel. Also shown are the individual best-fit model profiles for each phase (blue dashed) in addition to profiles corresponding to the model that provides the global maximum likelihood (red dotted) obtained from fits to the mean Stokes *V* profiles with $B_d = 10200$ G and $\beta = 7°$. The phase and best-fit parameters are also indicated for each observation.
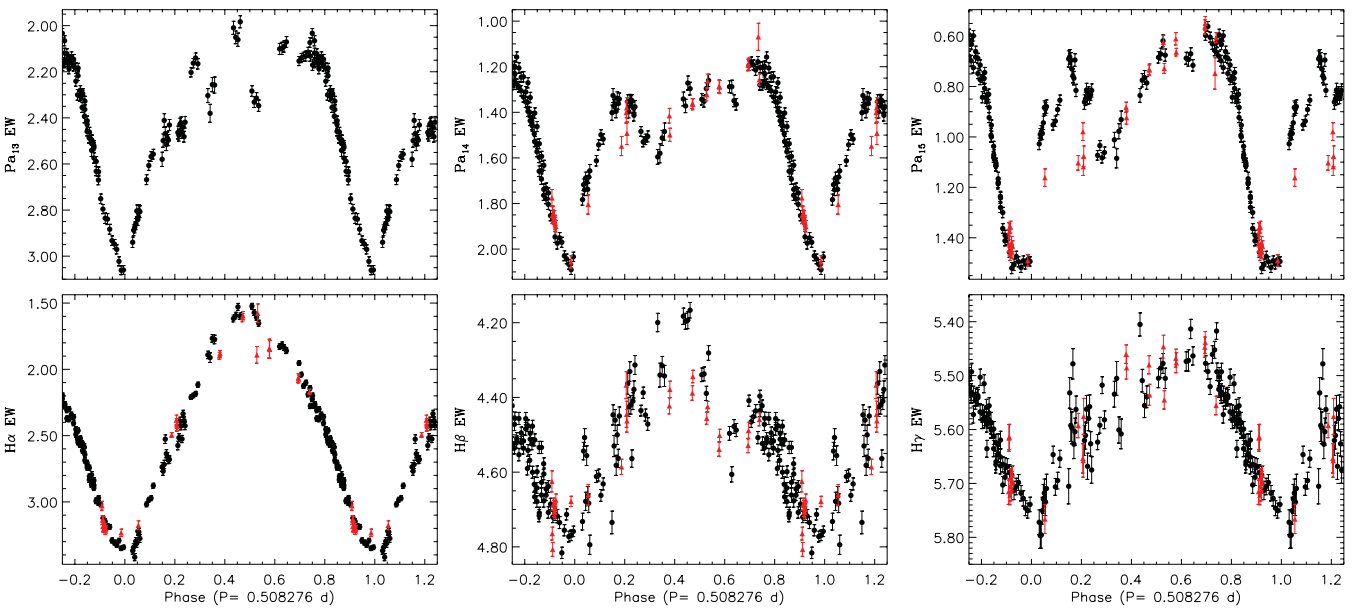
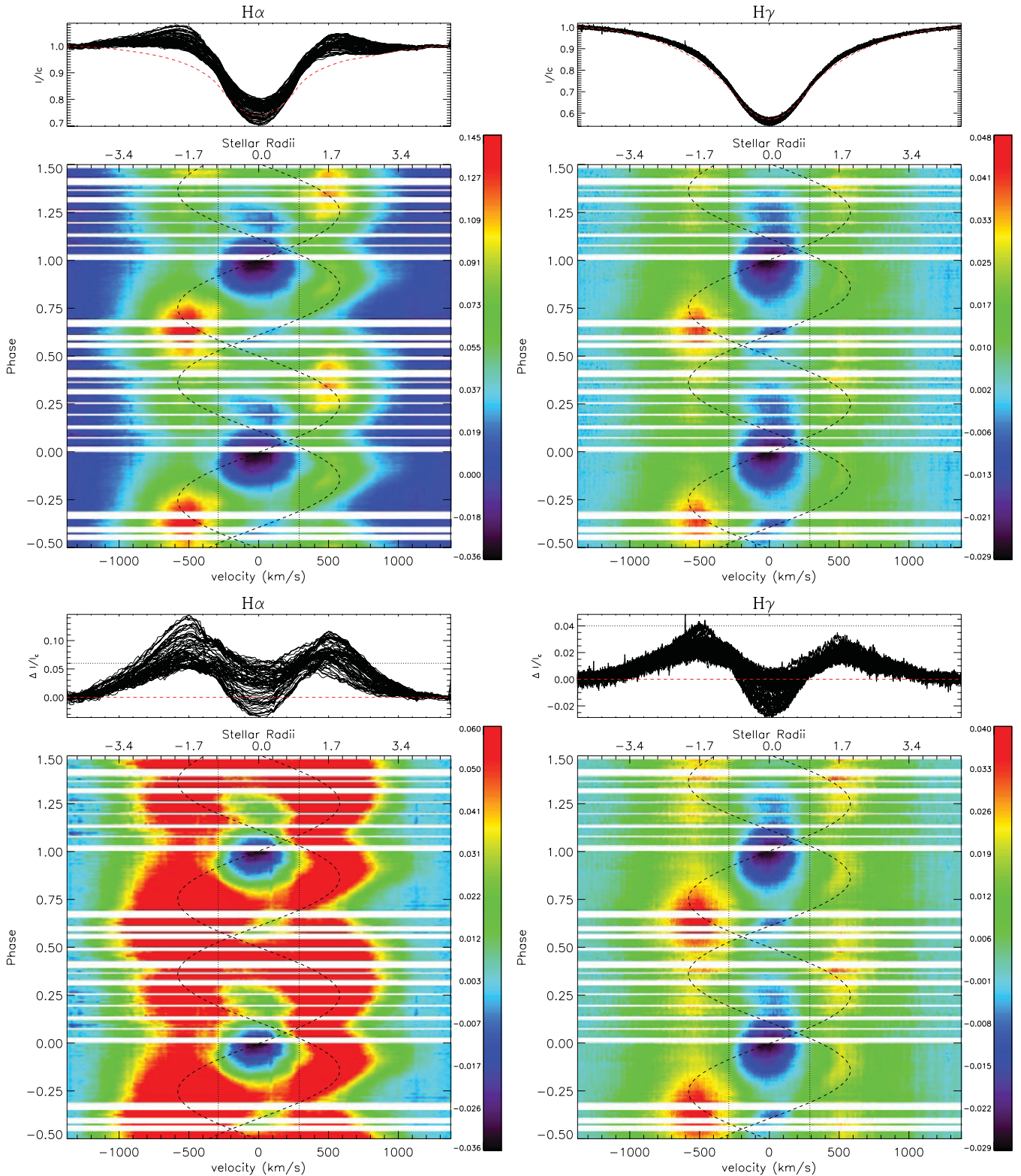**Figure 14.** Phased EW variations of hydrogen lines.

Figure 15. Phased observational variations of the circumstellar magnetosphere. Shown are the variations in the indicated Balmer lines after subtracting the best-fitting BK3 photospheric model (dashed red). The upper panels have a colour scheme chosen to show the full dynamic range of the emission variation, while the dynamic range in the lower panels are chosen to highlight the emission (green to red) features versus absorption (blue to black) features. Also shown are dashed vertical lines to indicate the rotational velocity (and radius) of HR 5907 and dashed curves to highlight the motion of the emission features as discussed in the text.
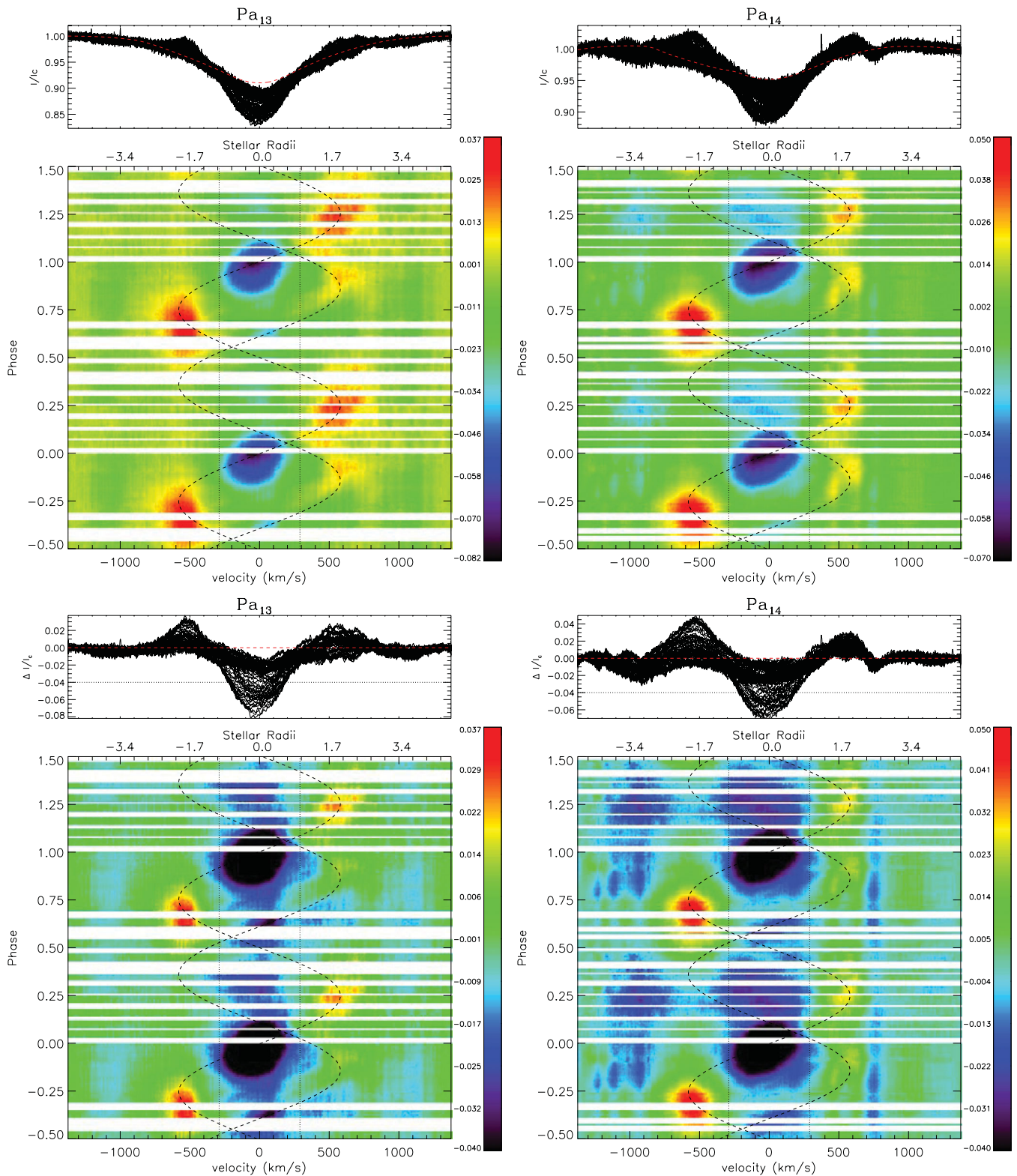
Figure 16. Phased observational variations of the circumstellar magnetosphere. Shown are the variations in the indicated Paschen lines after subtracting the best-fit TLUSTY photospheric model (dashed red). The upper panels have a colour scheme chosen to show the full dynamic range of the emission variation, while the dynamic range in the lower panels are chosen to highlight the emission (green to red) features versus absorption (blue to black) features. Also shown are dashed vertical lines to indicate the rotational velocity (and radius) of HR 5907 and dashed curves to highlight the motion of the emission features as discussed in the text.

From the Hα dynamic spectra we find that the main occultation occurs at phase 0.0, travelling redward. If we interpret this feature as a dense cloud in the circumstellar environment, then the fact that the occultation occupies a relatively broad velocity range during the eclipse indicates the cloud is azimuthally extended. Immediately following the broad absorption feature is a narrower feature that is still in emission in Hα (as highlighted in the bottom panel of Fig. 15), but is in absorption in Hγ and the Paschen lines of Fig. 16. This feature is travelling blueward and crosses $v_{sys} = 0\,\mathrm{km\,s^{-1}}$ at phase 0.21. Another occultation is clearly visible in the dynamic spectrum of Hγ moving redward and crossing $v_{sys} = 0\,\mathrm{km\,s^{-1}}$ at phase 0.59. Two clear emission peaks are also visible; the first feature appears at positive velocities, with the centre of the feature occurring at phase 0.36. A second blueward feature occurs at phase 0.62. We have included curves in Figs 15 and 16 that indicate the potential orbit for a given cloud if it is in rigid rotation. The curves were selected such that they pass through the blueward-migrating occultation and reach the same velocity extreme as the brightest emission features in the Paschen lines (which approximately correspond to the Kepler radius; see Section 8 for further details). From these orbital curves it seems likely that these two features are the same cloud viewed at opposite sides of the star, but the expected phase difference should be 0.5 and not 0.31 as measured. The mismatch between these curves and the migrating features seen in the dynamical spectra suggests that the features do not trace single, discrete clouds in the rigidly rotating magnetosphere, but rather arise from the combined effects of multiple, optically thick clouds distributed over a range of azimuths. The observed discrepancy between the maximum emission of this cloud at opposite quadratures is also qualitatively explained if the cloud is optically thick. Another redward emission feature is also visible, reaching a maximum redward velocity at phase 0.90 in Hα and Hγ. This feature appears to be related to the blueward emission feature that is more visible in Hγ at phase 0.38. If we interpret the emission features resulting from two distinct emission clouds in the circumstellar disc, it would imply that the clouds have a phase separation of ∼0.6.

In the dynamic spectra of the Paschen lines (Fig. 16) we still see the same basic features as found in the dynamic spectra of the Balmer lines – two strong emission features, followed by a third weaker feature. However, the phases at which the emission features occur are not consistent with the phases as observed in the Balmer lines. The centre of the first redward emission feature is observed at phase 0.23, the blueward feature is found to occur at phase 0.66, and the last redward feature is found at phase 0.91. The differences in the relative phasing of the features may be a result of subtracting the TLUSTY model and not the corresponding BK3 model, but this is unexpected as the locations of these emission peaks are far in the wings where the TLUSTY models provide the best fit to the BK3 models. There also appears to be a large disagreement in the phase difference between maximum emission, which cannot be due to using a TLUSTY model, as this is a constant spectrum subtracted from all models. The phase difference between the first redward feature and the blueward feature is 0.31 for the Balmer lines, but 0.43 in the Paschen lines. The phase difference between the blueward feature and the second redward emission peak is only 0.25 from the Paschen lines, compared to 0.28 from the Balmer lines. We believe the differences between the Balmer and Paschen dynamic spectra reflect their differing optical depths; the Paschen lines are (relatively) less optically thick, and therefore come closer to tracing individual clouds in the magnetosphere.

Since we know the circumstellar material is bound in co-rotation, we can unambiguously map radial velocity on to the projected stellar

surface, as indicated by the upper horizontal axis in Figs 15 and 16. With this information, we can now measure the furthest extent of the magnetospheric emission from the centre of the star. We find that the emission extends out to a maximum distance of 3.8 R_{eq} at phase 0.39, 4.4 R_{eq} at phase 0.59, and 4.2 R_{eq} at phase 0.93, as measured from the Hα dynamic spectrum. The middle of both redward features is found to occur at a distance of ∼1.7 R_{eq}, while the blueward feature is found to occur at a distance of 1.9 R_{eq}.

We also estimated the density in the circumstellar environment following the procedure of Štefl et al. (2003). Using the BK3 model as a good approximation of the photospheric profiles, we estimated the Balmer decrements D_{34} and D_{54} during phases where there is no apparent absorption in the dynamic spectra of Hα ($\phi = 0.45, 0.72$), from the residuals of the observed minus theoretical EWs, corrected to absolute flux using $f_\star(H\alpha)/f_\star(H\beta) = 0.36$ and $f_\star(H\gamma)/f_\star(H\beta) = 1.44$, as measured from the BK3 model. The Balmer decrements were then converted to densities using the theoretical computations of Williams & Shipman (1988), which were derived for an isothermal, pure hydrogen accretion disc of 10 000 K (the derived densities are weakly dependent on the temperature), which is optically thin in the continuum.

From these measurements, we find that the logarithmic density ranges from 11.3 to 13.5 particles per cm³. There is a large discrepancy between the logarithmic densities derived using D_{34}, which give a value of 13.5 at both phases, compared to values computed from D_{54} (11.3, 11.6). We speculate that the difference may be due to the poor normalization of the blue wing of the Hβ line and that the EW measurements of this line do not span the same velocity range as the other Balmer lines, since part of the blue wing of this line is not covered over a single order in the ESPaDOnS spectra. Another possibility is that the magnetospheric densities are very near the optically thick limit, or more likely straddling this limit, above which the measured Balmer decrements become independent of the density.

8 DISCUSSION AND CONCLUSIONS

This paper reports extensive spectroscopic and magnetic monitoring of the rapidly rotating, early B-type star HR 5907, based on UVES and FORS data obtained at the VLT, ESPaDOnS data from the CFHT, and MOST photometry. These observations and their analysis were undertaken within the context of the Magnetism in Massive Stars (MiMeS) Project.

We combined newly measured MOST photometry with archival *Hipparcos* measurements to refine the photometric period of this star to ∼0.508 276 d. A period search on the spectropolarimetric data confirms this period is also present in the EW variations of Hα as well as the longitudinal magnetic field measurements. If we interpret these observations within the context of the ORM with a rigidly rotating magnetosphere, then this period represents the rotation period of the star. A comparison of the Hα EW curve and photometric light curve suggests that there is ∼0.05 phase offset between the minima. This phase offset is not a result of a potentially incorrect period, as this would only affect the relative phasing between the *Hipparcos* photometry and the current epoch of observations and this offset is still present between the MOST photometry and Hα EW curve, indicating that there is a real phase shift between the observed minima. As with the differences between the Balmer and Paschen line profile variability, the phase shift likely arises from differences in optical depths of the continuum versus the Hα line.
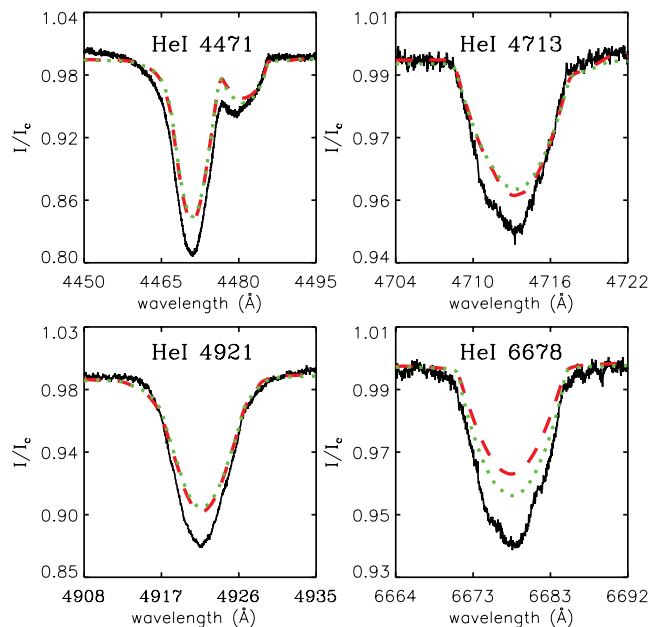
Figure 17. Comparison of observed helium lines (solid black; from 2010 February 24) with our best-fit solar abundance model ($T_{\rm eff} = 17\,{\rm kK}$, $M_\star = 5.5\,{\rm M_\odot}$, $R_{\rm eq} = 3.1\,{\rm R_\odot}$) computed in LTE (dashed red) and NLTE (dotted green). As the $T_{\rm eff}$ is independently constrained by the SED, this implies that HR 5907 is a He-strong star.

Using the optical spectroscopic data, archival *IUE* UV observations and the estimated rotation period, we were able to constrain the stellar physical parameters by comparing the spectra to a grid of BRUCE/KYLIE models (Townsend 1997), which properly reflect the oblateness of the star due to rapid rotation. The $T_{\rm eff}$ we find ($\sim$17 kK) is cooler than may otherwise be suggested by HR 5907's B2.5 spectral type, but can be understood if this star is actually a He-strong star. We believe this to be the case as the observed helium line depths are deeper than the modelled helium lines computed using solar abundances (as illustrated in Fig. 17). This would make HR 5907 similar to other magnetic early B-type stars. We speculate that the helium over-abundance in HR 5907's photosphere is likely the reason that other recent studies (Frémat et al. 2005) that use helium lines as a primary temperature indicator (even when taking into account rapid rotation) derive a much higher effective temperature ($\sim$21 250 K). We also investigated whether the discrepancy between the observed and modelled He lines was due to the assumption of LTE. Calculations using NLTE atmospheres (also displayed in Fig. 17) are not able to resolve the discrepancy.

As a final test, we determined the effective temperature that would be necessary to approximately fit the observed He line depths. The derived value is about 2 kK hotter than our adopted temperature (i.e. 19 kK). Such a temperature results in the C II 4267 Å line being about 25 per cent deeper, and the UV SED being about 20 per cent too large. Carbon abundances as measured from optical lines are poorly studied in Bp stars, but are typically found to be underabundant in cooler Ap stars (e.g. Roby & Lambert 1990). If $T_{\rm eff} = 19$ kK is adopted this would suggest that the carbon abundance would need to be reduced by 0.4 dex to fit the observed line depth, but this discrepancy will be somewhat mitigated if we use NLTE models, as the C II 4267 Å line is predicted to be weaker in NLTE, which would then increase the abundance necessary to fit the observed profile. However, adopting a NLTE model does not significantly affect the SED and the higher $T_{\rm eff}$ would provide a poorer fit to the UV SED. A

future self-consistent analysis that takes into account rapid rotation, NLTE effects, and non-solar He abundances is necessary to remove any ambiguity.

From the low-resolution FORS and high-resolution ESPaDOnS circular polarization measurements, we find that the mean, surface averaged, longitudinal magnetic field values are consistently negative. From the variation of these measurements we infer a dipolar magnetic field with a $\sim$16 kG field strength at the pole and a magnetic axis nearly aligned with the rotation axis ($\beta \sim 7^\circ$). However, direct modelling of the mean LSD profiles of the velocity-resolved Stokes *V* signatures suggests a lower dipole polar field strength of $\sim$10 kG. In any event, modelling of the circular polarization data shows large deviations from the simple dipole model at several rotational phases. These important deviations may indicate a more complex topology to the magnetic field structure, similar to what is seen in some other magnetic B-type stars. However, the observed deviations could also be due to the strongly variable helium lines that dominate our mean LSD profiles. In fact, the lower B_ℓ measurements around phase 0.5 are completely consistent with what is expected if helium is less abundant at the pole and therefore more weighted towards the equatorial regions where the helium lines are stronger. A self-consistent He-abundance and magnetic field map of the stellar surface, similar to HD 37776 (Kochukhov et al. 2011), is required to unambiguously determine the magnetic field topology of HR 5907.

Comparing the observed light curve with the photometric predictions of Townsend (2008), using our inferred inclination and magnetic obliquity, shows the two to be in good qualitative agreement. A lower inclination would not result in a perceivable dip in the light curve, unless the magnetic obliquity was about 30° or higher. On the other hand, if the inclination were higher, we would expect to see two dips in the lightcuve that would require a $\sim$1 d period (which would be inconsistent with the variations observed with the B_ℓ measurements) as opposed to the single dip that we do observe with our $\sim$0.5 d period. If the magnetic obliquity was much larger, we would expect to see two dips in the light curve, unless the inclination was lower.

As shown in Section 5, there appear to be significant chemical abundance variations across the stellar photosphere. Helium appears to have the strongest contrast, with EW variations on the order of 20 per cent, which is actually much smaller than observed in other rapidly-rotating He-strong stars such as σ Ori E or HR 7355. Carbon, silicon, and nitrogen are also found to vary weakly. In other He-variable stars the locations of these abundance spots are correlated with the magnetic field (e.g. Bohlender & Landstreet 1988) and usually axisymetric about the magnetic equator. Therefore the weak helium variability may well reflect the observed magnetic geometry - we are nearly always viewing the same orientation of the magnetic hemispheres and would expect only small rotational modulation since the magnetic axis is nearly aligned with the rotation axis. While the absolute helium variability might be weak compared to other rapidly-rotating He-strong stars, the helium surface distribution may vary enough to cause photometric fluctuations. The small dip that is evident in the photometric light curve (at about phase 0.65) also coincides with a small increase in helium absorption at this phase, as shown in Fig. 7.

Using the stellar parameters as derived in this paper and wind parameters estimated from these stellar parameters (included in Table 3 and obtained using formulae from Castor, Abbott & Klein (1975) and Vink, de Koter & Lamers (2001)), we find that the wind magnetic confinement parameter (ud-Doula & Owocki 2002) $\eta_* = B_{\rm eq}^2 R^2 / \dot{M} V_\infty \sim 10^6$, which indicates that the circumstellar material

Table 3. Summary of stellar, magnetic, wind and magnetospheric properties of HR 5907 derived in this work.

Stellar parameters	
Stellar mass ($M_\odot$)	5.5 ± 0.5
$T_{\rm eff}$ (K)	$17\,000 \pm 1000$
$\log(L_\star/L_\odot)$	2.78 ± 0.14
$P_{\rm rot}$ (d)	$0.508\,276^{+0.000\,015}_{-0.000\,012}$
$v_{\rm eq}\sin i$ (km s^{-1})	290 ± 10
Inclination ($^\circ$)	70 ± 10
Mass ($M_\odot$)	5.5 ± 0.5
Equatorial radius ($R_\odot$)	3.1 ± 0.2
$E(B-V)$	0.14
ω ($\Omega/\Omega_{\rm crit}$)	0.80
$v_{\rm eq}$ (km s^{-1})	309
Polar radius ($R_\odot$)	2.72
Polar temperature (K)	$18\,550$
Equatorial temperature (K)	$15\,920$
Log polar gravity (cm s^{-2})	4.31
Log equatorial gravity (cm s^{-2})	4.20
Magnetic parameters	
$B_{\rm d}$ (from B_ℓ) (kG)	$-15.7^{+0.9}_{-0.8}$
$B_{\rm d}$ (from LSD Stokes V) (kG)	$-10.4^{+0.4}_{-0.3}$
β ($^\circ$)	7^{+1}_{-2}
Wind properties	
$\log \dot{M}$ ($M_\odot$ yr^{-1})	-10
v_∞ (km s^{-1})	850
Magnetosphere properties	
η_*	$\sim 10^6$
$R_{\rm kep}$ ($R_{\rm eq}$)	2.0
$R_{\rm Alf}$ ($R_{\rm eq}$)	~ 31
Min extent of Hα emission ($R_{\rm eq}$)	~ 1.2
Max extent of Hα emission ($R_{\rm eq}$)	4.4
Log particle density (cm^{-3})	11.3–13.5
$\tau_{\rm spin}$ (Myr)	8

is strongly confined out to large distances from the star ($R_{\rm alf} = \eta_*^{1/4} \sim 30$–$40\,R_{\rm eq}$). The Kepler, or co-rotation, radius (ud-Doula et al. 2008) $R_{\rm kep} = 3/2\,\omega^{-2/3}\,R_{\rm pole} = 2.0\,R_{\rm eq}$, implying that beyond this radius, the material is centrifugally supported. We find that the locations of the emission peaks in Balmer and Paschen lines agree well with this value. We also computed the predicted spin-down time using equation (25) of ud-Doula, Owocki & Townsend (2009), $\tau_{\rm spin} \sim 8$ Myr, which is considerably longer than the potential age of HR 5907.

In summary, this study reports the detection of a large-scale, organized magnetic field with a polar surface intensity of 10–16 kG in HR 5907. Interpreted within the context of the ORM, we find photometric, Hα and longitudinal magnetic field variations consistent with a 0.508 276 d rotational period, making this the shortest period, non-degenerate, magnetic massive star known to date. We find evidence of surface abundance variations in helium, carbon, silicon and nitrogen.

This is one of only a few known rapidly rotating magnetic massive stars that show strong emission variations due to a magnetosphere. The only other massive star with a comparable rotation period is HR 7355, which is believed to have a magnetic geometry more similar to σ Ori E (a magnetic obliquity closer to 90°), which is very different from this star. HR 5907 is therefore an ideal target for comparison with the predictions of rigidly rotating magnetosphere models (Townsend & Owocki 2005; Townsend 2008) and a great testbed for studying the effects of the magnetic field orientation on angular momentum loss and magnetic spin-down.

REFERENCES

Bagnulo S., Szeifert T., Wade G. A., Landstreet J. D., Mathys G., 2002, A&A, 389, 191
Bagnulo S., Landolfi M., Landstreet J. D., Degl'Innocenti E., Fossati L., Sterzik M., 2009, PASP, 121, 993
Bertelli G., Nasi E., Girardi L., Marigo P., 2009, A&A, 508, 355
Bohlender D. A., Landstreet J. D., Brown D. N., Thompson I. B., 1987, ApJ, 323, 325
Bohlender D. A., Landstreet J. D., 1988, in Cayrel de Strobel G., Spite M., eds, Proc. IAU Symp. 132. The Impact of Very High S/N Spectroscopy on Stellar Physics, Kluwer, Dordrecht, p. 309
Borra E. F., Landstreet J. D., 1973, ApJ, 185, L139
Castor J. I., Abbott D. C., Klein R. I., 1975, ApJ, 195, 157
Cardelli J. A., Clayton G. C., Mathis J. S., 1989, ApJ, 345, 245
Donati J.-F., Semel M., Carter B. D., Rees D. E., Collier Cameron A., 1997, MNRAS, 291, 658
Donati J.-F., Babel J., Harries T. J., Howarth I. D., Petit P., Semel M., 2002, MNRAS, 333, 55
Donati J.-F., Howarth I. D., Bouret J.-C., Petit P., Catala C., Landstreet J., 2006, MNRAS, 365, L6
Frémat Y., Zorec J., Hubert A.-M., Floquet M., 2005, A&A, 305, 320
Hernández J., Calvet N., Hartmann L., Briceño C., Sicilia-Aguilar A., Berlind P., 2005, ApJ, 129, 856
Hoffleit D., Warren W. H., Jr., 1991, The Bright Star Catalogue, 5th edn. Yale Univ. Observatory, New Haven, CT
Hubert A. M., Floquet M., 1998, A&A, 335, 565
Hynes R., 2011, http://www.astro.soton.ac.uk/ rih/applets/MagCalc.html
Jaschek M., Egret D., 1982, ViZieR Online Data Catalogue
Kharchenko N. V., Roeser S., 2009, ViZieR Online Data Catalogue
Kochukhov O., Lundin A., Romanyuk I., Kudryatisev D., 2011, ApJ, 726, 24
Kurucz R. L., 1992, in Barbuy B., Renzini A., eds, The Stellar Populations of Galaxies Vol. 149 of IAU Symposium, Model Atmospheres for Population Synthesis. p. 225
Landstreet J. D., Borra E. F., 1978, ApJ, 224, L5
Lanz T., Hubeny I., 2007, ApJS, 169, 83
Lefèvre L., Marchenko S. V., Moffatt A. F. J., Acker A., 2009, A&A, 507, 1141
Leone F., Umana G., 1993, A&A, 268, 667
Lewis N. K., Cook T. A., Wilton K. P., France K., Gordon K. D., 2009, ApJ, 706, 306
Maeder A., Meynet G., 2010, NewAR, 54, 32
North P., Babel J., Lanz T., 1988, Inf. Bull. Var. Stars, 3155, 1
Oksala M. E., Wade G. A., Marcolino W. L. F., Grunhut J., Bohlender D., Manset N., Townsend R. H. D., 2010, MNRAS, 405, L510
Papaj J., Wegner W., Krelowski J., 1991, MNRAS, 252, 403
Pedersen H., Thomsen B., 1977, A&AS, 30, 11
Press W. H., Teukolsky S. A., Vetterling W. T., Flannery B. P., 1992, Numerical Recipes in FORTRAN, 2nd edn. Cambridge Univ. Press, Cambridge
Reiners A., Stahl O., Wolf B., Kaufer A., Rivinius T., 2000, A&A, 363, 585

Rivinius T., Szeifert T., Barrera L., Townsend R. H. D., Štefl S., Baade D., 2010, MNRAS, 405, L46

Roby S. W., Lambert D. L., 1990, ApJS, 73, 67

Schwarzenberg-Czerny A., 1996, ApJ, 460, L107

Shore S. N., Brown D. N., Sonneborn G., Landstreet J. D., Bohlender D. A., 1990, ApJ, 348, 242

Shore S. N., Brown D. N., 1990, ApJ, 365, 665

Shore S. N., 1993, in Dworetsky M. M., Castelli F., Faraggiana R., eds, ASP Conf. Ser. Vol. 44, Peculiar Versus Normal Phenomena in A-type and Related Stars. Astron. Soc. Pac., San Francisco, p. 528

Silvester J. et al., 2009, MNRAS, 398, 1505

Smith M. A., Bohlender D. A., 2007, A&A, 475, 1027

Townsend R. H. D., 1997, MNRAS, 284, 839

Townsend R. H. D., Owocki S. P., 2005, MNRAS, 357, 251

Townsend R. H. D., 2008, MNRAS, 389, 559

ud-Doula A., Owocki S. P., 2002, ApJ, 576, 413

ud-Doula A., Owocki S. P., Townsend R. H. D., 2008, MNRAS, 385, 97

ud-Doula A., Owocki S. P., Townsend R. H. D., 2009, MNRAS, 392, 1022

van Leeuwen F., 2007, A&A, 474, 653

Vink J. S., de Koter A., Lamers H. J. G. L. M., 2001, A&A, 369, 574

Štefl S., Baade D., Rivinius T., Otero S., Stahl O., Budovičová A., Kaufer A., Maintz M., 2003, A&A, 402, 253

Wade G. A. and the MiMeS Collaboration, 2011, proceedings of "Magnetic Stars", Special Astrophysical Observatory, preprint (arXiv :1012.2925)

Walborn N. R., 1982, PASP, 94, 322

Williams G. A., Shipman H. L., 1988, ApJ, 326, 738

This paper has been typeset from a TEX/LATEX file prepared by the author.